Icarus 411 (2024) 115922

Contents lists available at ScienceDirect

Icarus

journal homepage: www.elsevier.com/locate/icarus

Research Paper

NEOMOD 2: An updated model of Near-Earth Objects from a decade of Catalina Sky Survey observations

David Nesvorný [a,*], David Vokrouhlický [b], Frank Shelly [c], Rogerio Deienno [a], William F. Bottke [a], Eric Christensen [c], Robert Jedicke [d], Shantanu Naidu [e], Steven R. Chesley [e], Paul W. Chodas [e], Davide Farnocchia [e], Mikael Granvik [f,g]

[a] Department of Space Studies, Southwest Research Institute, 1050 Walnut St., Suite 300, Boulder, CO 80302, USA
[b] Institute of Astronomy, Charles University, V Holešovičkách 2, CZ–18000, Prague 8, Czech Republic
[c] Lunar and Planetary Laboratory, The University of Arizona, 1629 E. University Blvd., Tucson, AZ 85721-0092, USA
[d] Institute for Astronomy, University of Hawaii, 2680 Woodlawn Drive, Honolulu, HI 96822-1839, USA
[e] Jet Propulsion Laboratory, California Institute of Technology, 4800 Oak Grove Dr. Pasadena, CA 91109, USA
[f] Department of Physics, University of Helsinki, P.O. Box 64, FI-00014, Finland
[g] Asteroid Engineering Laboratory, Luleå, University of Technology, Box 848, SE-981 28, Kiruna, Sweden

ARTICLE INFO

Keywords:
Asteroids(72)
Near-Earth objects(1092)
Asteroid dynamics(2210)
Lunar impacts(958)
Tidal disruption(1696)

ABSTRACT

Catalina Sky Survey (CSS) is a major survey of Near-Earth Objects (NEOs). In a recent work, we used CSS observations from 2005–2012 to develop a new population model of NEOs (NEOMOD). CSS's G96 telescope was upgraded in 2016 and detected over 10,000 unique NEOs since then. Here we characterize the NEO detection efficiency of G96 and use G96's NEO detections from 2013–2022 to update NEOMOD. This resolves previous model inconsistencies related to the population of large NEOs. We estimate there are 936 ± 29 NEOs with absolute magnitude $H < 17.75$ (diameter $D > 1$ km for the reference albedo $p_V = 0.14$) and semimajor axis $a < 4.2$ au. The slope of the NEO size distribution for $H = 25$–28 is found to be relatively shallow (cumulative index $\simeq 2.6$) and the number of $H < 28$ NEOs ($D > 9$ m for $p_V = 0.14$) is determined to be $(1.20 \pm 0.04) \times 10^7$, about 3 times lower than in Harris & Chodas (2021). Small NEOs have a different orbital distribution and higher impact probabilities than large NEOs. We estimate 0.034 ± 0.002 impacts of $H < 28$ NEOs on the Earth per year, which is near the low end of the impact flux range inferred from atmospheric bolide observations. Relative to a model where all NEOs are delivered directly from the main belt, the population of small NEOs detected by G96 shows an excess of low-eccentricity orbits with $a \simeq 1$–1.6 au that appears to increase with H ($\simeq 30\%$ excess for $H = 28$). We suggest that the population of very small NEOs is boosted by tidal disruption of large NEOs during close encounters to the terrestrial planets. When the effect of tidal disruption is (approximately) accounted for in the model, we estimate 0.06 ± 0.01 impacts of $H < 28$ NEOs on the Earth per year, which is more in line with the bolide data. The impact probability of a $H < 22$ ($D > 140$ m for $p_V = 0.14$) object on the Earth in this millennium is estimated to be $\simeq 4.5\%$.

1. Introduction

NEOMOD is an orbital and absolute magnitude model of NEOs (Nesvorný et al., 2023, hereafter Paper I). To develop NEOMOD, we closely followed the methodology from previous studies (Bottke et al., 2002; Granvik et al., 2018), and improved it when possible. First, massive numerical integrations were performed for asteroid orbits escaping from eleven main belt sources. Comets were included as the twelfth source. The integrations were used to compute the probability density functions (PDFs) that define the orbital distribution of NEOs (perihelion distance $q < 1.3$ au, $a < 4.2$ au) from each source. Second, we developed a new method to accurately calculate biases of NEO surveys and applied it to the Catalina Sky Survey (CSS; Christensen et al., 2012) in an extended magnitude range ($15 < H < 28$). The publicly available `objectsInField`[1] code (`oIF`) from the Asteroid Survey Simulator (AstSim) package (Naidu et al., 2017) was used to determine the geometric bias of CSS. Third, we used the `MultiNest` code, a Bayesian

* Corresponding author.
E-mail address: davidn@boulder.swri.edu (D. Nesvorný).

[1] https://github.com/AsteroidSurveySimulator/objectsInField.

[2] https://www.boulder.swri.edu/~davidn/NEOMOD_Simulator and GitHub.

https://doi.org/10.1016/j.icarus.2023.115922
Received 12 October 2023; Received in revised form 27 November 2023; Accepted 11 December 2023
Available online 13 December 2023

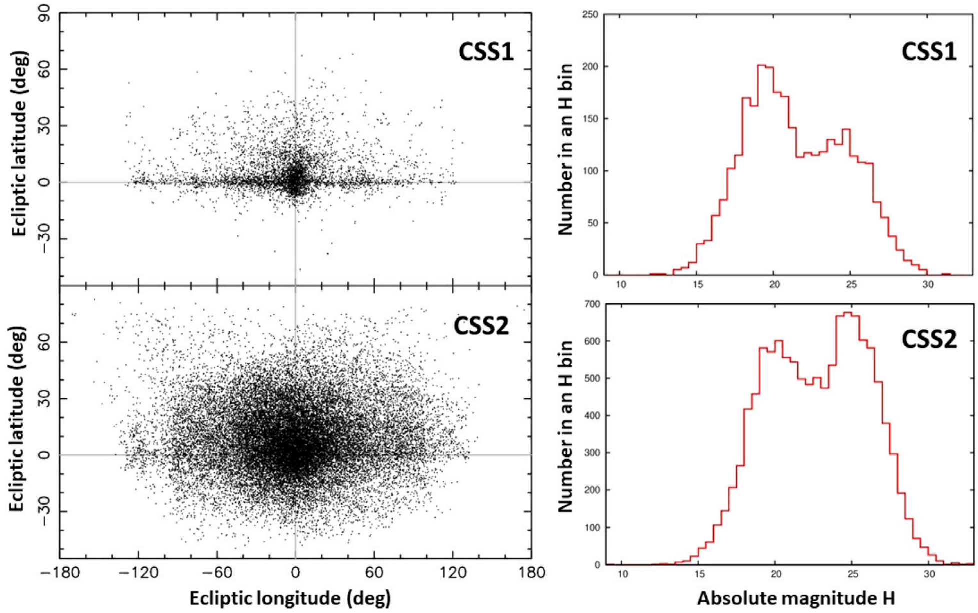

Fig. 1. NEOs detected by CSS1 (2013–2016; upper panels) and CSS2 (2016–2022; lower panels). The plots on the left show the ecliptic coordinates of detected objects. The plots on the right show their absolute magnitude distributions.

inference tool designed to efficiently search for best-fitting solutions in high-dimensional parameter space (Feroz and Hobson, 2008; Feroz et al., 2009), to optimize the biased model fit to CSS detections. The final model was made available to the scientific community via a NEOMOD Simulator[2] — an easy to operate code that can be used to generate user-defined NEO samples from the model.

The original model, hereafter NEOMOD v1.0 or NEOMOD1 for short, was calibrated on the Mt. Lemmon (IAU code G96) and Catalina (703) telescope observations during the 8-year long period from 2005 to 2012. This was done for two reasons: (1) the photometric sensitivity of G96 and 703 from 2005–2012 was thoroughly characterized in Jedicke et al. (2016), and (2) Granvik et al. (2018) used the same dataset to calibrate their NEO model. We improved the methodology and applied it to the same dataset, without the need for an extensive work on characterizing the photometric bias. The differences between NEOMOD1 and Granvik et al. (2018) therefore entirely reflected the changes in methodology (and not observational constraints). The improvements included: (i) cubic splines to represent the magnitude distribution of NEOs, (ii) rigorous model selection with `MultiNest`, (iii) a physical model for disruption of NEOs at low perihelion distances (Granvik et al., 2016), (iv) an accurate estimate of the impact fluxes on the terrestrial planets, and (v) a flexible setup that can be readily adapted to any current or future NEO survey.[3]

We found that the sampling of main-belt sources by NEOs is *size-dependent* with the ν_6 and 3:1 resonances contributing $\simeq$30% of NEOs with $H = 15$, and $\simeq$80% of NEOs with $H = 25$. This trend most likely arises from how the small and large main-belt asteroids reach the source regions (Paper I). The size-dependent sampling suggests that small terrestrial impactors preferentially arrive from the ν_6 source, whereas the large impactors can commonly come from the middle/outer belt (Nesvorný et al., 2021). The NEOMOD1-inferred contribution of the 3:1 source to large NEOs ($H \lesssim 18$) implies that main-belt asteroids should drift toward the 3:1 resonance at the maximum Yarkovsky drift rates ($\simeq 2 \times 10^{-4}$ au Myr^{-1} for a $\simeq$1-km diameter body at 2.5 au). In Paper I, we therefore suggested that the main-belt asteroids on the sunward side of the 3:1 resonance ($a < 2.5$ au) have obliquities $\theta \simeq 0°$; the ones with $a > 2.5$ au should have $\theta \simeq 180°$ (in the immediate neighborhood of the resonance). These predictions were confirmed from lightcurve observations (Ďurech and Hanuš, 2023). We verified the size-dependent disruption of NEOs at small perihelion distances (Granvik et al., 2016), and found a similar dependence of the disruption distance on the absolute magnitude.

Here we extend NEOMOD to incorporate new data from the G96 telescope (hereafter NEOMOD v2.0 or NEOMOD2 for short). The camera of G96 was upgraded to a wider field of view (FoV; $2.23° \times 2.23°$) in May 2016 and the G96 telescope detected 11,934 unique NEOs between May 31, 2016 and June 29, 2022 (Fig. 1). This can be compared to only 2987 unique NEO detections of G96 for 2005–2012 ($1.1° \times 1.1°$ FoVs). For completeness, we also include 3057 unique NEO detections of G96 between January 2, 2013 and May 16, 2016. The two new observational datasets are referred to as the "new CSS", whereas the previous dataset used in Paper I is the "old CSS". We do not attempt to combine the old and new CSS datasets in this work, because here we develop a new method for characterizing the photometric bias of new CSS (Section 2), and we do not want to mix the old and new approaches. The detection statistics of new CSS is large enough for the new CSS to stand on its own. The 703 telescope did not detect a comparatively large number of unique NEOs since 2013 and is not included here.

This article is structured as follows. In Section 2, we describe how the photometric bias was characterized for the new CSS. Section 3 briefly reviews the methodology that was borrowed from Paper I, including the definition of NEO sources, N-body integrations, choices of model parameters, and model optimization with `MultiNest`. The final model, NEOMOD2, synthesizes our current knowledge of the orbital and absolute magnitude distribution of NEOs (Section 4). We demonstrate that the population of very small NEOs detected by G96 shows an excess for low-eccentricity orbits with $a \simeq$ 1–1.6 au and suggest that the excess can be explained if large NEOs tidally disrupt during close encounters to the terrestrial planets (Section 5). Planetary impacts are discussed in Section 6.

2. Characterizing the observational bias of new CSS

The G96 telescope has a carefully recorded pointing history, amounting to over 240,000 frames for the 2013–2022 period. Here

[3] NEOMOD calibration on the ATLAS (Heinze et al., 2021) and WISE (Mainzer et al., 2019) observations is under development.

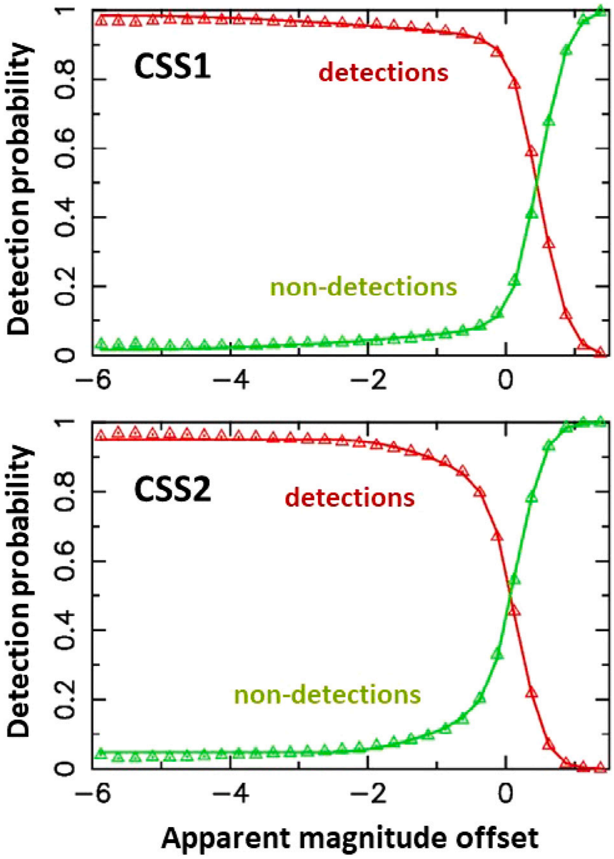

Fig. 2. Global photometric sensitivities of CSS1 (top panel) and CSS2 (bottom panel). The red triangles show the binned detection probability, $\epsilon(V') = N_{\rm det}(V')/N_{\rm all}(V')$ (Eq. (2)), as a function of the apparent visual magnitude offset V' (Section 2.1). The green triangles show the probability of non-detection, $1-\epsilon(V')$. The red and green lines show the best fits to the binned data using the functional dependence given in Eq. (2). (For interpretation of the references to color in this figure legend, the reader is referred to the web version of this article.)

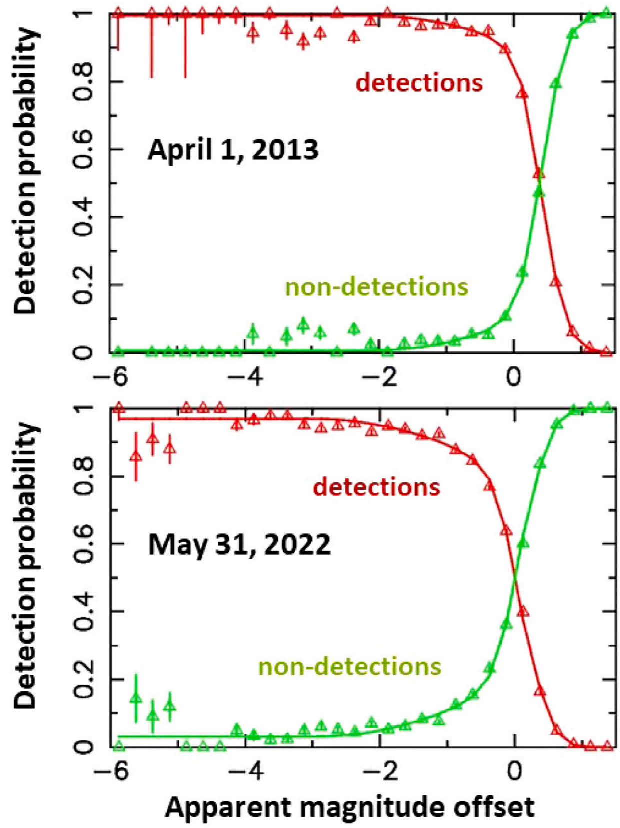

Fig. 3. Examples of nightly photometric detection probabilities for CSS1 (April 1, 2013; top panel) and CSS2 (May 31, 2022; bottom panel). See the caption of Fig. 2 for the description of symbols and lines. The error bars were estimated adopting the Poisson statistics.

we use new detections and incidental redetections of NEOs by CSS. We count each individual NEO only once (i.e., as detected) and do not consider multiple (incidental or not) detections of the same object. With this setup, we mainly care about the detection *probability* of an object by CSS, and not about the number of images in which that same object was detected (cf. Granvik et al. (2018)). The detection probability (or bias for short) of a moving object is defined as the probability that the CSS detection pipeline picks up an object in at least three images with the same pointing direction taken by CSS in short succession on a single night (image set or frame). The three (or more) tracklets must be correctly linked to count as true detection. The detection probability can be split into three parts: (i) the geometric probability of the object to be located in the image set, (ii) the photometric efficiency of detecting the NEO's tracklet, and (iii) the trailing loss. To account for (i), we use the publicly available `objectsInField`[4] code (`oIF`) from the Asteroid Survey Simulator (AstSim) package (Naidu et al., 2017). See the GitHub documentation of oIF for a detailed description of the code and Paper I for the implementation used here for NEO modeling.

As for (ii), our starting point is a 3.5 GByte tarball of nearly 10 years of data from the G96 telescope. To make this tarball, each G96 field was calibrated against Gaia-DR2 stars (Gaia Collaboration et al., 2018) and the moving object identification was done against the most recent MPCORB catalog (as of October 2022). For each frame, a list is provided of both the objects that were identified in the G96 image, and those that were expected to be in the field of view but were not detected. The data start on January 2, 2013 and end on June 29, 2022. There is one file per set of images with the same pointing direction taken by G96 in a short succession on the same night. The header of each file reports: the (1) exposure (typically 30 s, occasionally 45 s), (2) number of images in the frame (3 to 5, typically 4), (3) MJD when each image was taken, (4) right ascension and declination of the image center, (5) image orientation relative to north (always <1 deg), and (6) 50% magnitude value (V_{50}). The 50% magnitude value is a variation on a zero-point magnitude calculation. We collected all Gaia-DR2 stars that can be identified and scaled them against the matching point source SNR values converted to Δmag. The 50% value is the magnitude where the Gaia-DR2 stars cross an SNR that has been calibrated to give us roughly a 50% main belt asteroid detection rate as determined from a test set used at the time. It is a good reference to understand the quality of observing conditions for each frame.

Each file lists all *known* main-belt and near-Earth asteroids – obtained from the MPC catalog from October 2022 – that would appear in G96's frame that night, and specifies whether they were detected by the CSS pipeline. The following information is given for each object: the (1) proper motion (ω), (2) visual and absolute magnitudes (V and H), and (3) semimajor axis (a), eccentricity (e), and inclination (i). The V magnitude was computed from the observing geometry and H magnitude reported in the MPC catalog. We discarded nights where fewer than 250 asteroids were available (detected or not) in all frames taken on the same night of observations (18,509 files in total), because such a small number of objects did not allow us to accurately derive the

4 https://github.com/AsteroidSurveySimulator/objectsInField.

detection efficiency for that night (Section 2.1). We also excluded 27 files with fewer than three images per frame (three images are required for detection). This left us with 223,865 files in total (one file for each exposure), 61,585 for nights before May 16, 2016 (hereafter CSS1) and 162,280 after May 31, 2016 (hereafter CSS2).

The unique NEO detections were extracted from all files. If the same object was detected more than once, we only considered the first instance. NEOs detected on discarded nights were neglected. We also excluded NEO detections with $w > 10$ deg/day because we were not able to determine the trailing loss for these excessively large apparent motions (Section 2.2). This left us with 2619 unique NEOs for CSS1 and 11,471 unique NEOs for CSS2 (objects detected by both CSS1 and CSS2 are listed twice, once in each dataset; Fig. 1). The two datasets report the semimajor axis, eccentricity, inclination, and absolute magnitude of the NEOs (at the time of detection). Note that the H magnitudes of all objects were obtained from the 2022 MPC catalog (downloaded on October 19, 2022); this defines the absolute magnitude system used in this is work.[5] Given the previously identified offset of MPC magnitudes (Pravec et al., 2012), the 2022 MPC system may still include systematic errors. In addition, as the absolute magnitudes of individual objects are updated with each new release of the MPC catalog, one has to be careful when comparing the NEOMOD2 results with new MPC releases.

2.1. Photometric probability of detection

We adopt the following method to characterize the photometric probability of detection. For each asteroid reported in each file, we first compute the visual magnitude offset $V' = V - V_{3rd}$, where V_{3rd} is the third faintest 50% magnitude value listed in the frame file header (V_{50}).[6] The reason for the 3rd faintest is that it takes at least three hits for a detection. The 3rd faintest field therefore has the main impact on the efficiency. All asteroids appearing in the same frame, detected or not, are binned as a function of V', defining $N_{all}(V')$. We also bin the number of asteroids *detected* by the G96 pipeline and denote it by $N_{det}(V')$. The photometric probability of detection in a V' bin is simply the ratio $\epsilon(V') = N_{det}(V')/N_{all}(V')$. We use 30 bins between $V'_{min} = -6$ and $V'_{max} = 1.5$ (i.e., bin size 0.25 mag). This is where practically all NEOs were detected by G96. We therefore do not need to characterize the detection efficiency for $V' < V'_{min}$ and $V' > V'_{max}$.[7]

In the next step, we need to find a suitable analytic expression that provides a sufficiently good approximation for $\epsilon(V')$. This is a matter of compromise. On one hand, there is a preference for a simple and robust approximation that will always provide a reasonable approximation of binned $\epsilon(V')$, even if the statistics on a given night is relatively poor. On the other hand, the analytic function must be sufficiently accurate in the whole range $V'_{min} < V' < V'_{max}$, including the transition where $\epsilon(V')$ drops near the detection limit, such that no artifacts are introduced. The original functional form that was adopted in Paper I from Jedicke et al. (2016) was

$$\epsilon(V) = \frac{\epsilon_0}{1 + \exp\left(\frac{V - V_{lim}}{V_{wid}}\right)} . \tag{1}$$

After extensive testing, we adopted

$$\epsilon(V') = \epsilon_0 \frac{1 - \left(\frac{V' - V'_0}{q_V}\right)^2}{1 + \exp\left(\frac{V' - V'_{lim}}{V_{wid}}\right)^{\alpha}} . \tag{2}$$

We now use $V' = V - V_{3rd}$ instead of V in Eq. (2). There are six parameters: ϵ_0, V'_0, q_V, V'_{lim}, V_{wid} and α. The α parameter improves the analytic fit for $V' \to V'_{max}$, where $\epsilon(V')$ rapidly drops toward zero. The 'squeezed' exponential with $\alpha > 1$ for $V' > V'_{lim}$ matches this fall off better than a normal exponential. This behavior cannot be mimicked by adopting a smaller value of V_{wid} because this would damage the fit for $V' < V'_{lim}$ (we fix $\alpha = 1$ for $V' < V'_{lim}$). The quadratic term in the numerator of Eq. (2) was taken from Tricarico (2016). It improves the behavior of the analytic fit for $V'_0 < V' < V'_{lim}$, where $\epsilon(V')$ has a bending profile that differs from an exact exponential. When the statistics on a given night is relatively small (i.e., low N_{all}), the bins near V'_{min} are sparsely filled, and this would adversely affect the quadratic term, if the fit is given this much freedom. For $V' < V'_0$, where $V'_{min} < V'_0 < V'_{lim}$ is a free parameter of the fit, we therefore set $\epsilon(V') = \epsilon_0$.

The optimization of six photometric parameters was performed with the Simplex method (Press et al., 1992). We have the capability to execute the fit for one frame, for all CSS observations (Fig. 2), and everything in between. We find that the number of asteroids in a single frame is typically too small for a robust determination of $\epsilon(V')$ in each frame. We therefore need to group frames together. Grouping too many frames together would not be optimal, however, because the atmospheric conditions may significantly vary between different nights, the observing strategy and parameters change over time, etc. We thus choose to characterize $\epsilon(V')$ on a nightly basis (see Fig. 3 for an example).

All frames taken on a single night were collected, the offset $V' = V - V_{3rd}$ was applied individually for each frame, but the binning and Simplex fit were done only once for the whole night. We discarded nights with $N_{all} < 250$ because we did not have confidence in the results when the total asteroid sample on that night was small. The six photometric parameters were individually obtained for 602 nights of CSS1 and 1110 nights of CSS2 (Fig. 4). Table 1 lists the global photometric parameters for CSS1 and CSS2 for reference. In general, CSS2 has brighter values of V'_{lim} than CSS1. This means that, for CSS2, V_{3rd} is a better proxy for where the photometric detection efficiency drops. The V_{3rd} values of CSS2 are generally fainter, by a fraction of magnitude, than those of CSS1. We stress that, even if the six photometric parameters ϵ_0, V'_0, q_V, V'_{lim}, V_{wid} and α have fixed values for a given night, V_{3rd} is treated individually for each frame. We therefore have an approximate characterization of the photometric efficiency on a frame-to-frame basis.[8]

2.2. Trailing loss

The trailing loss stands for a host of effects related to the difficulty of detecting fast moving objects. If the apparent motion is high, the object's image (a streak) is smeared over many CCD pixels, which diminishes the maximum brightness and decreases S/N. Long trails may be missed by the survey's pipeline (due to streaking), the object may not be detected in three images of the same frame (as required for a detection), or the streaks in different images may not be linked

[5] The absolute magnitudes of the detected NEOs were given to two decimal digits but the second decimal digit was often zero. This happened because the legacy MPC catalogs, from which some data were imported, listed only one decimal digit. As this would create round-off problems with binning, we randomly added −0.001 or +0.001 to the reported magnitudes. This resolves the problem.

[6] We use the usual Pogson's relation to compute the visual magnitude of each object. Nominally, we set the slope parameter $G = 0.15$ (Bowell et al., 1989) but also tested $G = 0.24$ (Pravec et al., 2012). The results described in Section 4 are practically independent of this choice.

[7] There were some exceptions such as (433) Eros; objects detected with $V' > V'_{min}$ or $V' < V'_{max}$ were discarded.

[8] Note that the method described here accounts for the reduction of the detection probability from the camera's *fill* factor — the fraction of the FoV where camera is actually sensitive (parts of the camera are not sensitive because of gaps, masked pixels, etc.). The fill factor is implicitly accounted for as the detection probability is inferred from detections and non-detections of *real* objects appearing in each image.

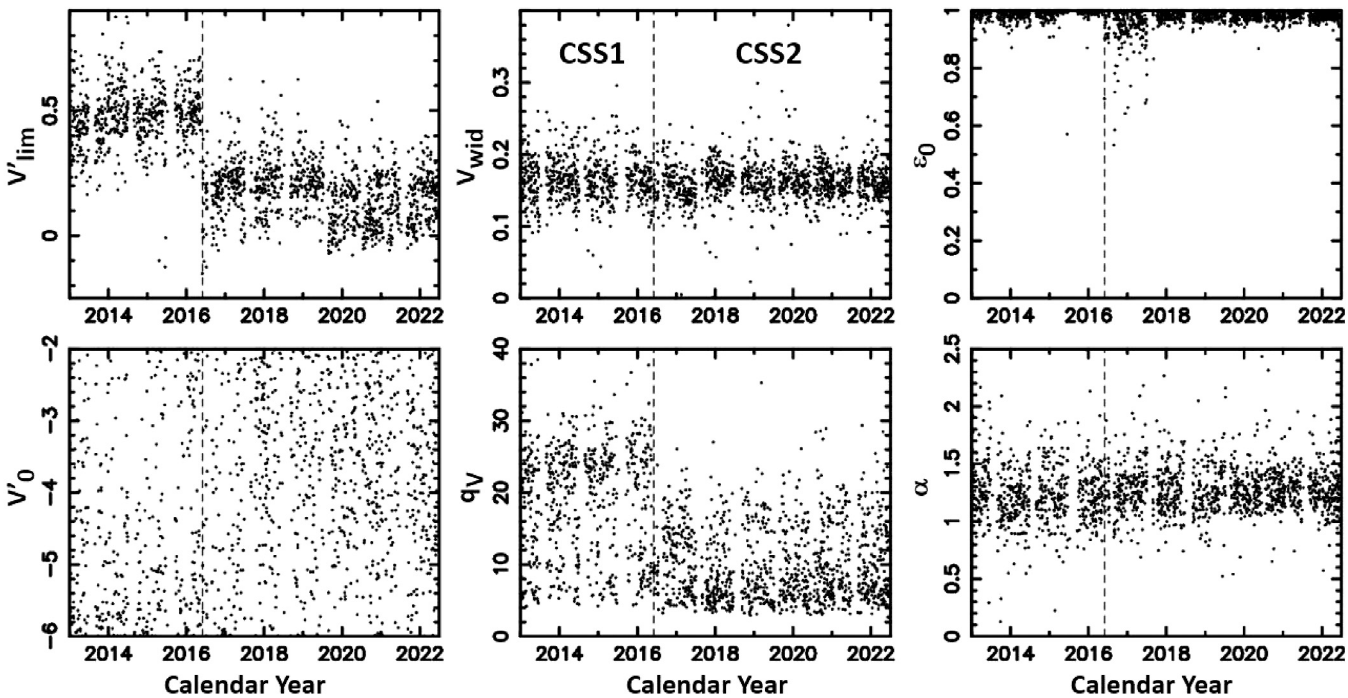

Fig. 4. Variation of six photometric parameters (Eq. (2)) derived on a nightly basis, for the whole duration of new CSS (January 2013 to June 2022). The G96 telescope was upgraded in May 2016 (vertical dashed lines).

Table 1
Global photometric parameters of CSS1 and CSS2. See Section 2.1 and Eq. (2) for the definition of these parameters: ϵ_0 defines the detection efficiency for bright apparent magnitudes, V'_0 and q_V are parameters of the quadratic term that improve the behavior of the analytic fit for $V' < V'_{\rm lim}$, $V'_{\rm lim}$ is the apparent magnitude where the detection efficiency drops, $V_{\rm wid}$ defines how fast it drops, and α improves the behavior of the analytic fit for $V' > V'_{\rm lim}$. CSS2 has a lower value of global $V'_{\rm lim}$ than CSS1. This means that, for CSS2, $V_{\rm 3rd}$ is a better proxy for where the photometric detection efficiency drops. The large value of CSS1's q_V reduces the importance of the quadratic term; this term is more important for CSS2. The values reported here were computed for the apparent motion $0.12 < w < 1$ deg/day.

	CSS1	CSS2
ϵ_0	0.983	0.952
V'_0	−6.0	−2.65
q_V	23.87	6.64
$V'_{\rm lim}$	0.475	0.170
$V_{\rm wid}$	0.180	0.175
α	1.140	1.151

together. The trailing loss is especially important for small NEOs, which can only be detected when they become bright, and this typically happens when they are moving very fast relative to Earth during a close encounter.

It is not easy to accurately characterize the trailing loss from the CSS data that are available to us. This is mainly because the number of detected objects in CSS frames rapidly falls off for high rates of motion. The statistics therefore becomes progressively worse as we consider higher and higher rates of motion. Ideally, we would like to investigate different effects (see above) separately, because some should vary with cadence, while the trailing loss itself (smearing) depends on the angular velocity. This is unfortunately not possible because there is simply not enough data for high rates of motion. In addition, we would like to characterize the trailing loss on a nightly basis, on a monthly basis, or at least separating CSS1 and CSS2. This is also not possible because there is not a sufficient number of detections in CSS1 for $w > 3$ deg/day.

We therefore adopt the following (approximate) procedure. We first clump all the CSS1 and CSS2 observations together and separate $N_{\rm all}$ and $N_{\rm det}$ into 1 deg/day bins in the apparent motion, from $w = 0$ to $w = 10$ deg/day. There are only under 200 unique detections in individual bins for $w > 10$ deg/day, and that is clearly not good enough for characterizing the trailing loss. The asteroids detected with $w > 10$ deg/day were discarded from the detection probability computation and from the list of detected NEOs. We only consider $w < 10$ deg/day. With the w binning, the detection efficiency is now $\epsilon(V', w)$. As before (Section 2.1), we use the Simplex method and Eq. (2) to analytically parameterize $\epsilon(V', w)$, and derive the six photometric parameters, which are now global for the new CSS, but depend on w. The photometric parameters were plotted as a function of w to give us sense of how they change and what analytic functions would capture that behavior.

An example for $V'_{\rm lim}(w)$ is shown in Fig. 5. Even though the dependence of $V'_{\rm lim}$ on w is uneven, we find that $V'_{\rm lim}(w)$ slightly increases to $w \simeq 3.5$ deg/day and then drops for $w > 3.5$ deg/day. This means that the detection efficiency improves for the apparent motions approaching $w \simeq 3.5$ deg/day, which corresponds to $\simeq$3 pixels/exposure for CSS2. Confusion of moving objects with faint stars probably decreases the detection rates for very slow apparent motions.[9] As we go faster than 3 pixels/exposure there is a double penalty of losses from trailing and the increased angular distance between the first and last point (which makes it more difficult to uniquely link the observations to a moving object). That could explain why $V'_{\rm lim}(w)$ slopes downward for $w > 3.5$ deg/day.

We analytically approximate $V'_{\rm lim}(w)$ as

$$V'_{\rm lim}(w) = V'_{\rm lim}(0) + Aw \tag{3}$$

for $w < w_1$ and

$$V'_{\rm lim}(w) = V'_{\rm lim}(0) + Aw_1 + 2.5\log_{10}[1 + C(w - w_1)] \tag{4}$$

[9] We looked into this in more detail and found that the CSS2 detection probability drops for $w < 0.12$ deg/day. This happens because an object moving this slow appears in only a few pixels of the image set, and this greatly diminishes its detection probability. We therefore used $w > 0.12$ deg/day for the computation of $\epsilon(V')$ in Section 2.1. According to our tests, however, including $w < 0.12$ deg/day would not have a significant impact on the overall results described in Section 4.

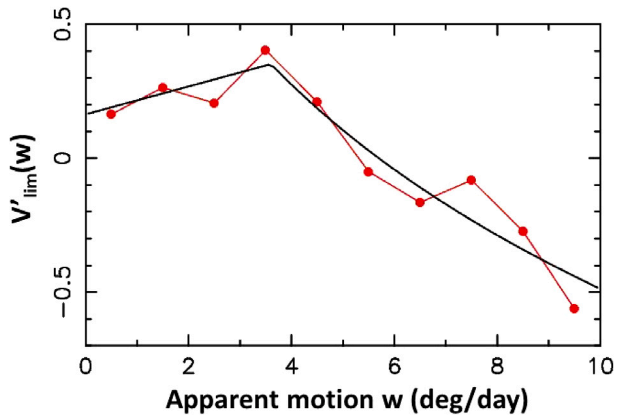

Fig. 5. The dependence of the transition magnitude $V'_{\rm lim}$ on the asteroid's apparent motion w. The red line and dots show $V'_{\rm lim}(w)$ obtained from the Simplex fit to all new CSS observations. The black line is the analytic fit with the functional form described in the main text (Eqs. (3) and (4)).

for $w_1 < w < 10$ deg/day, and find $A = 0.052$, $C = 0.192$, $w_1 = 3.6$ deg/day. To respect the photometric conditions of each night, we set $V'_{\rm lim}(0)$ to be equal to $V'_{\rm lim}$ derived for that night (top-left panel of Fig. 4).

The functional form of trailing loss in Eq. (4) was obtained from the following reasoning. Let ϕ be the characteristic angular dimension of the point spread function (PSF). Let the angular rate of motion of the object be w during an exposure time t. Assume that trailing effects only become important after an object has moved through an angle $\theta = w_1 t$ where w_1 is identified as the minimum rate of motion at which trailing loss becomes apparent. Let the flux within the PSF from a stationary source be $f_s = 1$. If the same source is moving at a rate w for a time t across the image plane, its flux will be spread along a trail of angular length $\ell = \phi + wt$. Then the flux within a PSF area along the trail is roughly

$$f_t = \frac{\phi + (w - w_1)t}{\phi} = 1 + \frac{t}{\phi}(w - w_1). \tag{5}$$

Thus, the change in apparent magnitude in a PSF-like region due to trailing is given by

$$\Delta V = 2.5 \log_{10}\left[1 + \frac{t}{\phi}(w - w_1)\right]. \tag{6}$$

A good rule-of-thumb is that w_1 is the rate at which an object moves a full PSF during the exposure time. The G96 PSF is roughly $3''$ and $t = 30$ s, so we expect $w_1 \sim 2.4$ deg/day and $\frac{t}{\phi} \sim 0.42$ day/deg, in rough agreement with the fitted values (see above).

In an actual survey system there are many different, often competing, factors at play in the detection efficiency including, but not limited to, the ability of the system's software to detect sources in an image as a function of the source's shape and an object's rate of motion. Distant objects, or even nearby objects at their stationary points, may move too slowly to be detected as moving between successive images. Sources that trail just a little might be easier to detect than sources that trail a little less. These effects are difficult to calculate from theory so we generalize the trailing loss function in Eq. (4) and fit for the parameters A, C and w_1.

A similar analysis was performed for other photometric parameters as well. We found that $V_{\rm wid}(w)$ can be adequately approximated by $V_{\rm wid}(0)$ for $w < w_2$ with $w_2 \simeq 7$ deg/day. For $w > w_2$, the transition from high to low detection probabilities near $V'_{\rm lim}(w)$ becomes a step-like function; we thus have $V_{\rm wid} = 0$ for $w > 7$ deg/day. The last issue arises as there were no objects detected for V' exceeding a certain limit, $V'_{\rm cut}$, where $V'_{\rm cut} = 1.5$ mag for $w \simeq 0$ (our usual cutoff) and $V'_{\rm cut} = 0$ when w approaches 10 deg/day. In the final algorithm for the trailing loss, we implemented this cutoff by setting $\epsilon(V') = 0$ for $V' > V'_{\rm cut}$.

2.3. Detection probability as a function of a, e, i and H

The detection probability of new CSS, $\mathcal{P}(a, e, i, H)$, needs to be computed as a function of a, e, i and H. As we described in Paper I, the model distribution of NEO orbits is binned (we use the same binning as in Paper I). We therefore need to compute $\mathcal{P}(a, e, i, H)$ in each bin. For each bin, we generated a large number ($N_{\rm obj} = 10{,}000$; the required number was determined by convergence tests) of test objects with a uniformly random distribution of a, e and i within the bin boundaries. The mean anomaly, argument of perihelion, and longitude of ascending node were randomly chosen between 0 and 360°. The `oIF` code (Naidu et al., 2017) was then used to determine the geometric detection probability in each frame. For each H bin, we assigned the corresponding absolute magnitude to 10,000 test NEOs and propagated the information to compute the detection efficiency $\epsilon_{j,k}(V, w)$, individually for every bin j and frame k (Eq. (2) and Section 2.2). See Sect. 4.5 in Paper I for more details.

The detection probability $\mathcal{P}(a, e, i, H)$ is defined as the mean detection probability of an object with (a, e, i, H) over the whole duration of each survey. We compute the mean detection probability as

$$\mathcal{P} = \frac{1}{N_{\rm obj}} \sum_{j=1}^{N_{\rm obj}} \left\{ 1 - \prod_{k=1}^{N_{\rm frame}} [1 - \epsilon_{j,k}] \right\} , \tag{7}$$

where $N_{\rm frame}$ is the number of frames, and the product of $1 - \epsilon_{j,k}$ over frames stands for the probability of *non*-detection of the object j in the survey. We compute $\mathcal{P}$ separately for CSS1 and CSS2.

Figs. 6 and 7 illustrate the CSS bias. The detection probability of CSS2 is $\gtrsim 0.7$ for large, $H \simeq 15$ NEOs, except for those on orbits with $a < 0.8$ au. Fainter NEOs are detected with lower probability. Interestingly, $\mathcal{P}$ shows dips and bumps as a function of NEO's semimajor axis (Fig. 7). The dips, where the detection probability is lower, correspond to the orbital periods that are integer multiples of 1 year. This is where the synodic motion of NEOs allow them to hide and often not appear in the survey's frames. This effect has been reported before (Tricarico, 2017 and Paper I).

3. NEO model parameters and optimization

The source populations and integration method used to generate the orbital distribution of NEOs from each source were described in Paper I. We have 12 sources in total: eight individual resonances (ν_6, 3:1, 5:2, 7:3, 8:3, 9:4, 11:5 and 2:1), weak resonances in the inner belt, two high-inclination sources (Hungarias and Phocaeas), and comets. The integration output was used to define the binned orbital distribution of NEOs from each source j, $dp_j(a, e, i) = p_j(a, e, i)\, da\, de\, di$, and normalized it to one NEO,

$$\int_{a,e,i} p_j(a, e, i)\, da\, de\, di = 1 , \tag{8}$$

effectively representing the binned orbital PDF (probability density function). We used the orbital range $a < 4.2$ au, $q < 1.3$ au, $e < 1$ and $i < 90°$, hereafter the NEO model domain. This is where practically all NEOs detected by new CSS reside.[10] As the binning is done only in a, e, and i, the model ignores any possible correlations with the orbital angles (nodal, perihelion and mean longitudes). There are 42 bins in a, 20 bins in e and 22 bins in i, and 52 bins in H for $14 < H < 28$.

We use `MultiNest` to perform the model selection, parameter estimation and error analysis (Feroz and Hobson, 2008; Feroz et al., 2009).[11] `MultiNest` is a multi-modal nested sampling routine (Skilling, 2004) designed to compute the Bayesian evidence in a

[10] Exceptions are: (343158) Marsyas with a retrograde orbit and $a = 2.527$ au, (3552) Don Quixote, 2019 PR2, 2019 QR6 and three other (weakly active) comets on Jupiter-crossing orbits with $a > 4.2$ au.

[11] https://github.com/farhanferoz/MultiNest.

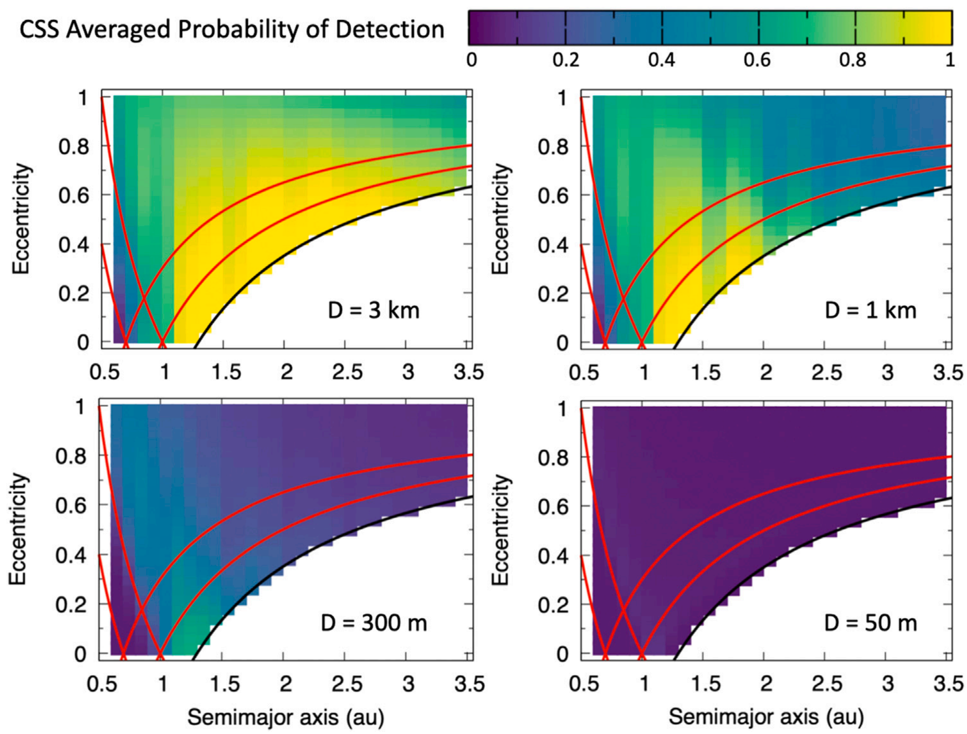

Fig. 6. The CSS2 detection probability (Eq. (7)) as a function of orbital elements for four different absolute magnitude values. From top-left to bottom-right, we plot $\mathcal{P}(a, e, i, H)$ for H corresponding to objects with $D = 3$ km, 1 km, 300 m and 50 m (for the reference albedo $p_V = 0.14$). The detection probability was averaged over all inclinations bins. The vertical strips, with $\mathcal{P}$ going up and down as a function of NEO's semimajor axis, are a consequence of the synodic effect (see discussion in Paper I). The red lines show borders of the orbital domain where orbits can have close encounters with Earth and Venus.

complex parameter space in an efficient manner. The log-likelihood in `MultiNest` is defined as

$$\mathcal{L} = \ln P = -\sum_j \lambda_j + \sum_j n_j \ln \lambda_j \ , \tag{9}$$

where n_j is the number of objects detected by CSS in the bin j, λ_j is the number of objects in the bin j expected from the biased model, and the sum is executed over all bins in a, e, i and H. This definition is identical to that used in Paper I. For two or more surveys, $\mathcal{L}$ is simply the sum of individual survey's log-likelihoods. As we treat CSS1 and CSS2 as two independent surveys, we have $\mathcal{L} = \mathcal{L}_{\rm CSS1} + \mathcal{L}_{\rm CSS2}$.

There are three sets of priors: (1) coefficients α_j that determine the strength of different sources, (2) parameters related to the absolute magnitude distribution, and (3) priors that define the disruption model (Granvik et al., 2016).

As for (1), the intrinsic orbital distribution of model NEOs is obtained by combining $n_{\rm s}$ sources: $p(a,e,i) = \sum_{j=1}^{n_{\rm s}} \alpha_j\, p_j(a,e,i)$ with $\sum_{j=1}^{n_{\rm s}} \alpha_j = 1$. The coefficients α_j represent the relative contribution of each source to the NEO population (i.e., the fraction of NEOs from the source j). As the contribution of different sources to NEOs may be size dependent (Paper I), we set α_j coefficients to be functions of the absolute magnitude. For simplicity, we adopt a linear relationship, $\alpha_j = \alpha_j^{(0)} + \alpha_j^{(1)}(H - H_\alpha)$, where H_α is some reference magnitude, and $\alpha_j^{(0)}$ and $\alpha_j^{(1)}$ are new model parameters. In practice, we set $\alpha_j(H_{\rm min})$ and $\alpha_j(H_{\rm max})$ for some minimum and maximum absolute magnitudes (e.g., $H_{\rm min} = 15$ and $H_{\rm max} = 28$), and linearly interpolate between them. This automatically assures that $\sum_j \alpha_j(H) = 1$ for any $H_{\rm min} \le H \le H_{\rm max}$.

As for (2), the differential and cumulative absolute magnitude distributions are denoted by $dn(H) = n(H)dH$ and $N(H)$, respectively. The differential magnitude distribution produced by source j is set to be $dn_j(H) = \alpha_j(H)n(H)dH$. The magnitude distributions of different sources are similar, but change with $\alpha_j(H)$, which are assumed to linearly vary with H (see above). When the contribution of different sources is combined, we find that $\sum \alpha_j(H)n(H)dH = n(H)dH$, which means that $n(H)$ stands for the absolute magnitude distribution of the whole NEO population.

We use cubic splines to represent $\log_{10} N(H)$ (Paper I). The magnitude interval of interest, $15 < H < 28$, is divided into six segments. There are six parameters defining the average slope in each segment, γ_j, and one parameter that provides the overall calibration. We use $N_{\rm ref} = N(H_{\rm ref})$ with $H_{\rm ref} = 17.75$ (diameter $D = 1$ km for the reference albedo $p_V = 0.14$). The normalization constant and slope parameters are used to compute $\log_{10} N(H)$ at the boundaries between segments; cubic splines are constructed from that (Press et al., 1992). The splines assure that $N(H)$ smoothly varies with H. The known sample of NEOs with $H < 15$ is thought to be (nearly) complete, and there were $\simeq$50 such objects in the MPC catalog from October 2022. We therefore fix $N(15) = 50$ and compute the γ_1 slope such that this additional constraint is satisfied.

As for (3), following Granvik et al. (2016), we eliminate test bodies when they reach the critical distance q^* (q^* is the perihelion distance below which NEOs completely disintegrate in catastrophic breakups). Here we assume that the q^* dependence on H is (roughly) linear, and parameterize it by $q^* = q_0^* + \delta q^*(H - H_q)$, where $H_q = 20$. We use uniform priors for the two parameters, q_0^* and δq^*. To construct the orbital distribution for any $q^* < 0.4$ au, we first produce the binned distributions (from each source) for $q^* = 0$, 0.05, 0.1, 0.15, 0.2, 0.25, 0.3, 0.35 and 0.4 au. The fitting routine then linearly interpolates between these distributions to any intermediate value of $q^*(H)$. The resulting orbital distribution, p_{q^*}, which now also depends on the absolute magnitude, $p_{q^*} = p_{q^*}(a,e,i,H)$, is normalized to 1 ($\int p_{q^*}(a,e,i,H)\, da\, de\, di = 1$ for any H).

In summary, our biased NEO model is

$$\mathcal{M}_{\rm b}(a,e,i,H) = n(H)\,\mathcal{P}(a,e,i,H) \sum_{j=1}^{n_s} \alpha_j(H)\, p_{q^*,j}(a,e,i,H) \ , \tag{10}$$

where α_j are the magnitude-dependent weights of different sources ($\sum_j \alpha_j(H) = 1$), n_s is the number of sources, $p_{q^*,j}(a,e,i,H)$ is the PDF of

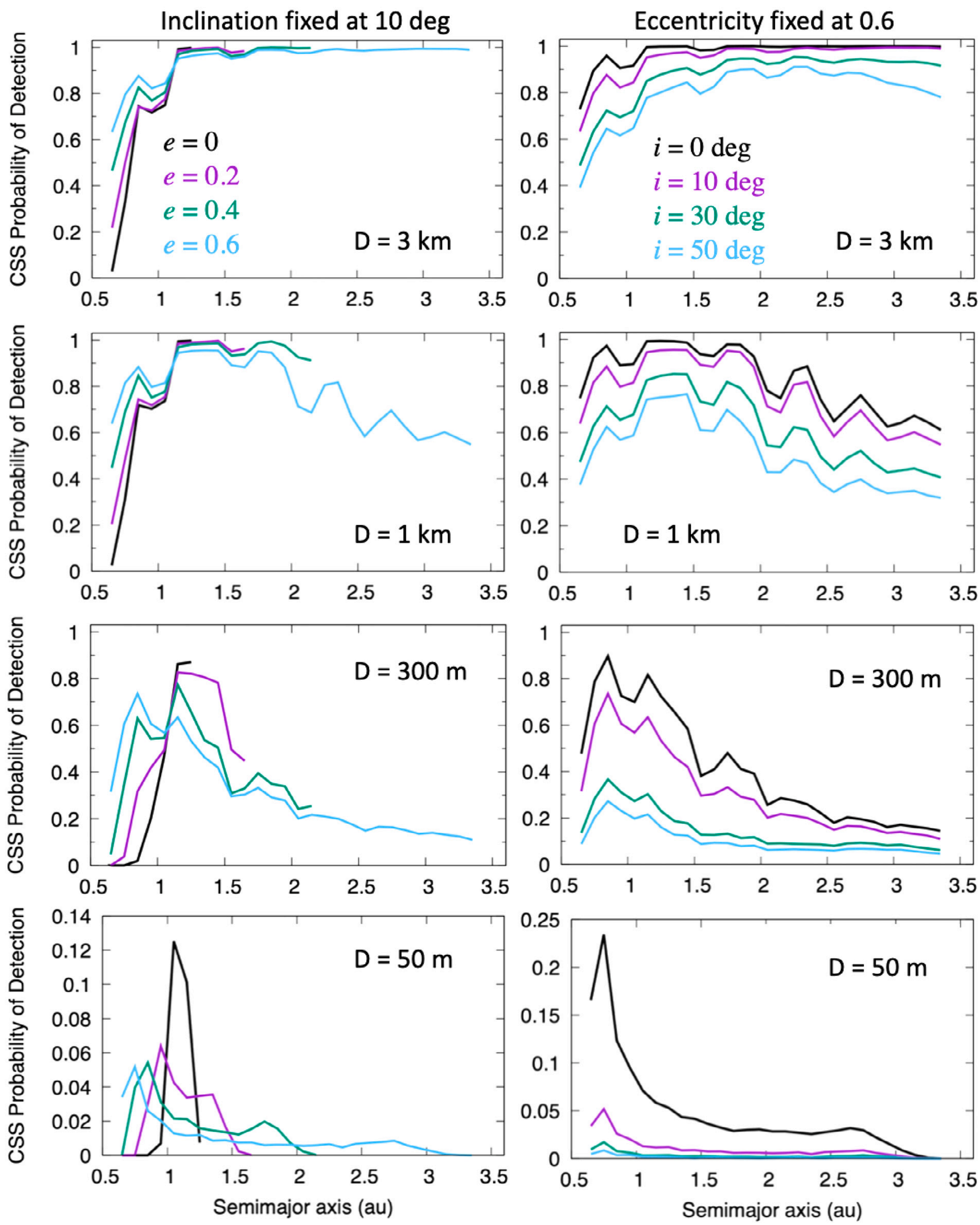

Fig. 7. The CSS2 detection probability (Eq. (7)) as a function of orbital elements for four different absolute magnitude values. From top to bottom, we plot $\mathcal{P}(a, e, i, H)$ for H corresponding to objects with $D = 3$ km, 1 km, 300 m and 50 m (for the reference albedo $p_V = 0.14$). The plots in the left column show $\mathcal{P}$ for the fixed orbital inclination ($i = 10°$) and several eccentricity values. The plots on the right show $\mathcal{P}$ for $e = 0.6$ and several inclination values. The detection probability was computed for orbits with $q < 1.3$ au.

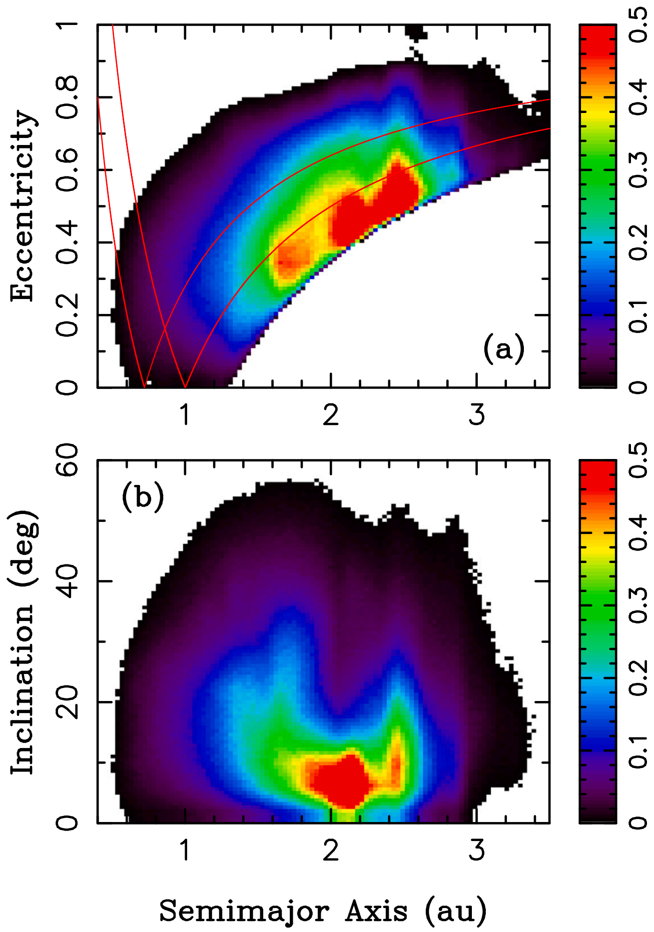

Fig. 8. The orbital distribution of NEOs from our *intrinsic* (debiased) best-fit model $\mathcal{M}$. We used the NEOMOD Simulator (Section 4) and generated 1.1×10^6 NEOs with $15 < H < 28$. The distribution was marginalized over absolute magnitude and binned using 100 bins in each orbital element ($0.4 < a < 3.5$ au, $e < 1$ and $i < 60°$). Warmer colors correspond to orbits where NEOs are more likely to spend time. The red lines show borders of the orbital domain where orbits can have close encounters with Earth and Venus. (For interpretation of the references to color in this figure legend, the reader is referred to the web version of this article.)

the orbital distribution of NEOs from the source j, including the size-dependent disruption at the perihelion distance $q^*(H)$ (this is the only H-dependence in the p functions), $n(H)$ is the differential absolute-magnitude distribution of the NEO population (the log-cumulative distribution is given by splines), and $\mathcal{P}(a, e, i, H)$ is the CSS detection probability (Eq. (7)). For each MultiNest trial, Eq. (10) is constructed by the methods described above. This defines the expected number of events $\lambda_j = \mathcal{M}_b(a, e, i, H)$ in every bin of the model domain, and allows MultiNest to evaluate the log-likelihood from Eq. (9).

The intrinsic (debiased) NEO model is simply

$$\mathcal{M}(a, e, i, H) = n(H) \sum_{j=1}^{n_s} \alpha_j(H)\, p_{q^*,j}(a, e, i, H) \ . \quad (11)$$

By integrating Eq. (11) over the orbital domain, given that $\int p_{q^*,j}(a, e, i, H)\, da\, de\, di = 1$ and $\sum_j \alpha_j(H) = 1$, we verify that $n(H)$ stands for the (differential) magnitude distribution of the whole NEO population.

4. NEOMOD v2.0

Our base NEO model accounts for $n_s = 12$ sources (Paper I). Each source has a magnitude-dependent contribution (Section 3) and the source weights $\alpha_j(15)$ (for $H = 15$) and $\alpha_j(28)$ (for $H = 28$) therefore represent $2(n_s - 1)$ model parameters (the last source's contribution is computed from $\sum_{j=1}^{n_s} \alpha_j = 1$). There are six parameters related to the magnitude distribution, $N_{\rm ref}$ and γ_j, $2 \leq j \leq 6$ ($15 \leq H \leq 28$).[12] The γ_1 parameter is fixed such that $N(15) = 50$. In addition, the q_0^* and δq^* parameters define the disruption model. This adds to 30 model parameters in total. We used uniform priors for all parameters (see Paper I for the multivariate uniform distribution of $\alpha_j(15)$ and $\alpha_j(28)$). The CSS fits were executed with the MultiNest code (Section 3). The orbital distribution of NEOs from the best-fit (i.e., highest-likelihood) intrinsic model $\mathcal{M}$ is shown in Fig. 8. The NEOMOD Simulator (see Paper I) was updated and is available for download.[13]

MultiNest provides the posterior distribution of model parameters. The results are generally consistent with those of Paper I, but there are also several interesting differences (Table 2). As before, we only have upper bounds on the contribution of 7:3, 9:4 and JFC sources. The models without these sources, however, are disfavored at $\Delta \ln \mathcal{Z} > 9.2$ (Bayes factor). We thus prefer to keep these sources in the base model. The ν_6 source now has a lower contribution for $H = 15$ (0.06 ± 0.03 vs. 0.12 ± 0.06 in Paper I) and a higher contribution for $H = 28$ (0.60 ± 0.02 vs. 0.42 ± 0.04 in Paper I). The opposite happens for the 3:1 resonance, which now has a 0.28 ± 0.03 contribution for $H = 15$ (previously 0.22 ± 0.04) and 0.31 ± 0.02 contribution for $H = 28$ (previously 0.34 ± 0.03). The contribution of Hungarias for $H = 28$ has an upper limit (0.029; previously 0.06 ± 0.03). These differences are most likely related to how the observations of 703 and G96 telescopes were combined in Paper I (see Section 8 in Paper I and the footnote below). The uncertainties of all parameters are lower than in NEOMOD1, typically by almost a factor of 2. The absolute magnitude and disruption parameters are similar to those reported in Paper I. We find $N(17.75) = 936 \pm 29$ (Table 3).[14]

The biased best-fit model $\mathcal{M}_b$ is compared to CSS NEO detections in Fig. 9. The distributions in Fig. 9 are broadly similar. There seems to be a slight excess of CSS NEO detections with $q \sim 1$ au and $1 < a < 1.6$ au. The 1D PDFs in Figs. 10 and 11 show the comparison in more detail. For relatively bright NEOs ($15 < H < 25$; Fig. 10), $\mathcal{M}_b$ is statistically indistinguishable from CSS detections. The Kolmogorov–Smirnov (K–S) test (Press et al., 1992), applied to the four 1D distributions in Fig. 10, shows that the null hypothesis (the distributions are drawn from the same underlying distribution) cannot be rejected (K–S probability $p > 0.05$). The troughs in the semimajor axis distribution at $a \simeq 1.6$ and 2.1 au are produced by the lower detection efficiency of CSS for orbital periods near 2 and 3 years (synodic effect; Fig. 7). The tiny excess of NEOs detected by CSS with $i = 20$–$30°$ (red line in Fig. 10c) can be related to the contribution of high-inclination sources (Hungarias or Phocaeas).

For faint NEOs ($25 < H < 28$; Fig. 11), $\mathcal{M}_b$ is indistinguishable from CSS detections in i and H, but there is a major discrepancy in a and e, where the CSS detections show a large excess for $1 < a < 1.6$

[12] We tested different sectioning of the magnitude range and found that having six intervals $H = 15$–16.5, 16.5–17.5, 17.5–20.0, 20.0–24.0, 24.0–25.0, and 25.0–28.0 works slightly better than having equal spacing.

[13] https://www.boulder.swri.edu/~davidn/NEOMOD_Simulator and GitHub.

[14] In Paper I, we experimented with two approaches to combining the data from the 703 and G96 telescopes. In the first one, inspired by Granvik et al. (2018), the detection biases of the two telescopes were combined into a joint survey (see Paper I for details). Strictly speaking, this is not ideal because the detection bias of the G96 survey only applies to NEO detections in the G96 survey (and not 703), and vice versa. We verified in Paper I that the joint-survey approach gives $N(17.75) < 1000$ (Granvik et al., 2018 estimated $N(17.75) = 962^{+52}_{-56}$) even if both 703 and G96 – when considered separately – give $N(17.75) > 1000$ (for old CSS and the bias from Jedicke et al. (2016)). In the second and more accurate method, 703 and G96 were treated separately in MultiNest and were combined at the log-likelihood level. This, however, produced $N(17.75) = 1010 \pm 19$ in Paper I. Here we find that these model inconsistencies most likely reflected a slight inaccuracy of the observational bias reported for old CSS in Jedicke et al. (2016).

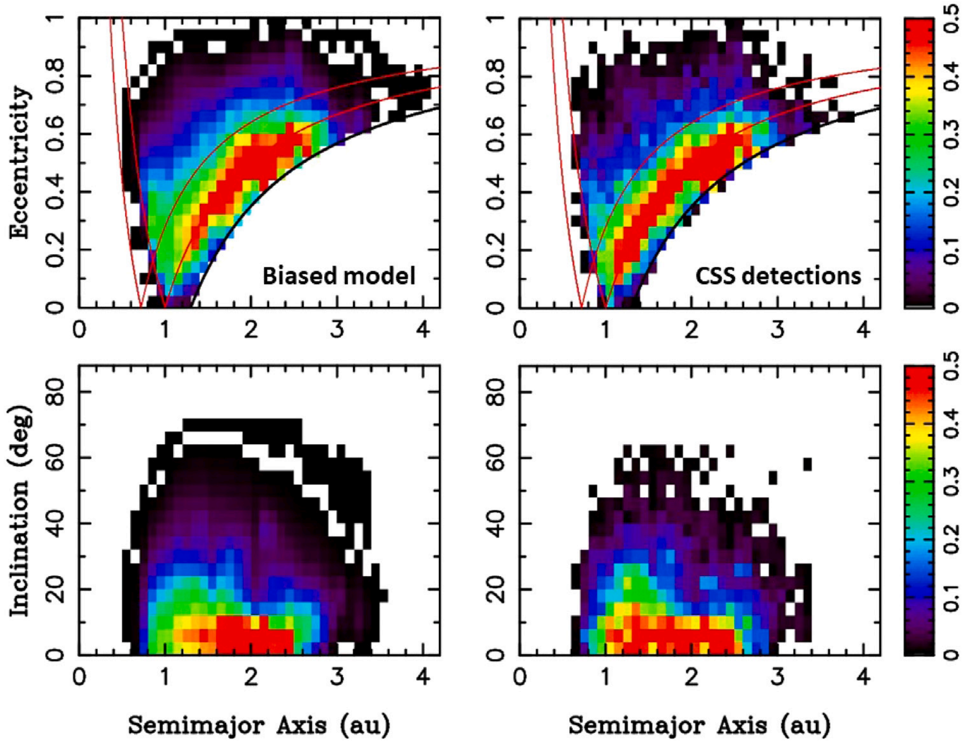

Fig. 9. The orbital distribution of NEOs from our *biased* best-fit model $\mathcal{M}_b$ (left panels) and the CSS NEO detections (right panels). The model distribution for $15 < H < 28$ was marginalized over absolute magnitude and binned with the standard resolution. It is shown here in the (a, e) and (a, i) projections. Warmer colors correspond to orbits where NEOs are more likely to be found. The red lines show borders of the orbital domain where orbits can have close encounters with Earth and Venus. The black line corresponds to $q = 1.3$ au. (For interpretation of the references to color in this figure legend, the reader is referred to the web version of this article.)

au and $e < 0.4$. The 1D K–S tests applied to the a and e distributions indicate that the null hypothesis can be rejected ($p < 10^{-5}$). The same problem was already discussed in Paper I, where we verified that the excess cannot be explained by a rapid drift of $D < 100$ m asteroids across the ν_6 resonance. The excess also cannot be related to disruption of NEOs at low perihelion distances (Granvik et al., 2016, and Paper I), because (i) NEOs with $1 < a < 1.6$ au and $e < 0.4$ do not reach very low perihelion distances, and (ii) we need to add objects to our model, and not remove them, to explain the excess of detections. This problem is most likely related to *tidal disruption* of large NEOs during planetary encounters (Granvik and Walsh, 2017, 2022, 2023); a relatively large fraction ($\simeq$20–30%) of small NEOs with $25 < H < 28$, $1 < a < 1.6$ au and $e < 0.4$ can be fragments of tidally disrupted NEOs. We discuss this issue in Section 5.

The intrinsic (debiased) absolute magnitude distribution from our base model $\mathcal{M}$ is shown in Fig. 12. It is nearly identical to that reported in Harris and Chodas (2021, hereafter HC21) for $H < 25$. There is a large difference between $\mathcal{M}$ and HC21 for $H > 25$, where the NEOMOD2 distribution has a well defined slope index $\gamma \simeq 0.51$ (equivalent to a power index $\simeq$2.6 of the cumulative size distribution). Here the distribution given in HC21 is significantly steeper ($\gamma \simeq 0.62$ for $24 < H < 27$ or even $\gamma \simeq 0.75$ for $H > 26$). The same discrepancy was already noted in NEOMOD1 — here we confirm it from a detailed analysis of new CSS. The slope of our size distribution for $H > 25$ is consistent with the slope expected for a population that reached the collisional equilibrium (Dohnanyi, 1969). The steeper slope in HC21 (cumulative size index $\simeq$3.75 for $H > 26$) would require some additional explanation.

For reference, HC21 obtained 2.44×10^7 NEOs with $H < 27.75$ whereas we only have $0.912{\times}10^7$ NEOs with $H < 27.75$ - a multiplicative factor of $\simeq$2.7 difference (Table 3). It is possible that we overestimated the CSS detection efficiency by a factor of $\sim$2–3 for $H \simeq 28$. If so, this would bring our magnitude distribution up by the same factor. We do not believe, however, that this is the case. For example, NEOMOD1 – where the detection efficiency was obtained for old CSS (2005–2012) from Jedicke et al. (2016) – produced practically the same result as we find here from the new analysis of new CSS (2013–2022). It would be strange if two observational datasets and two (independent) analyses of the detection efficiency produce the same error. It is also possible that the magnitude distribution reported in HC21, who based their estimate on NEO redetections and extrapolated it to $H > 25$, is too steep for $H > 25$.[15]

The redetection method is limited to a magnitude range where the numbers of new detections and redetections are statistically large ($17 \lesssim H \lesssim 24$; Harris and D'Abramo, 2015). To extrapolate the results to fainter magnitudes, HC21 assumed that a survey detects an increasingly smaller fraction of the NEO population and estimated – from the statistics of close encounters of faint NEOs to the Earth – that this fraction was proportional to $10^{-0.8H}$. The proportionality was further adjusted to $10^{-1.0H}$ for $H > 26$ to better fit bolide observations (Brown et al., 2002, 2013). But HC21 implicitly assumed, by anchoring the results to the redetection approach at $H \simeq 24$, that the orbital distributions of small and large NEOs are the same. We already showed in Paper I that they are not the same (also see Granvik et al. (2016, 2018)). Moreover, as we discuss in Section 5, tidal disruption of large NEOs produce small NEOs with orbits that have high probabilities of Earth encounters. It may therefore be somewhat problematic to

[15] Here we compare our results with the case from Harris and Chodas (2021) where NEOs with $H > 24$ were given the slope $1.0(V_{\rm lim} - H)$. This is the theoretically expected slope and the one that better connects to the bolide data (if a fixed impact probability is adopted, but see Section 6). Harris and Chodas (2021) pointed out that the slope $0.8(V_{\rm lim} - H)$ better matches the slope obtained from their redetection method near $H = 24$. This shallower slope for $H > 24$ would be in better agreement with our results.

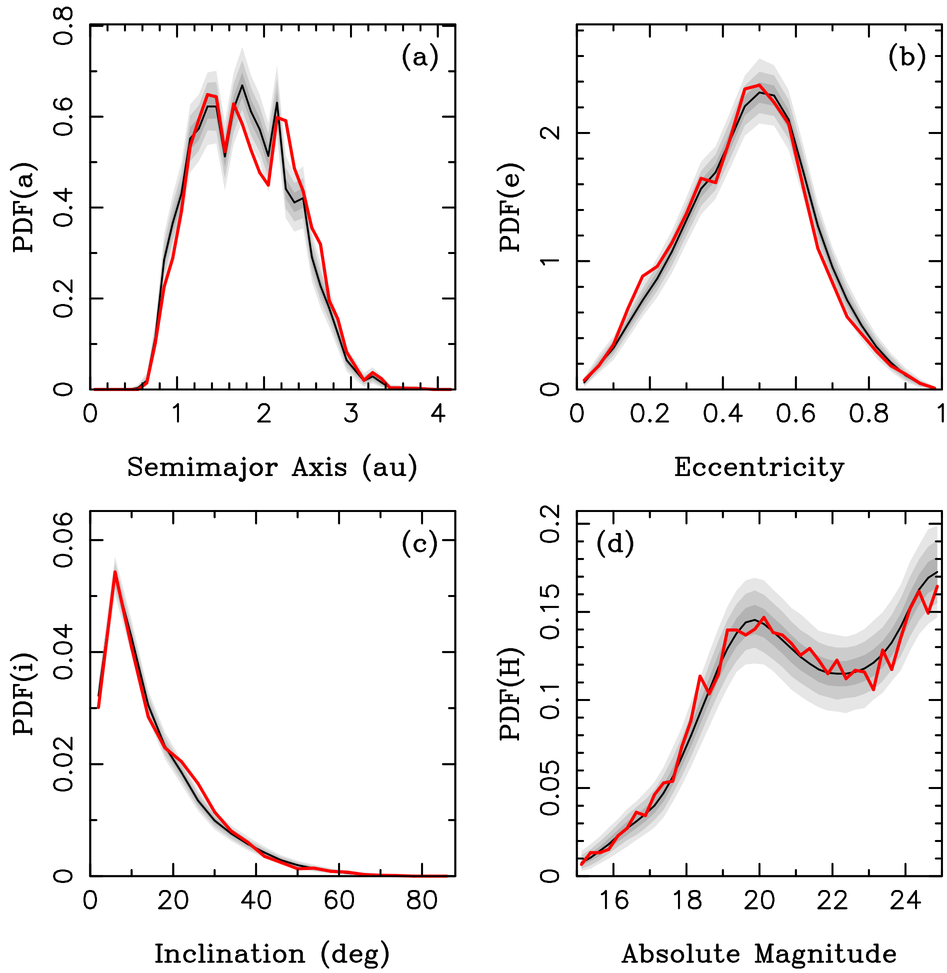

Fig. 10. The probability density functions (PDFs) of a, e, i, and H from our biased base model (black lines) and the CSS2 NEO detections (red lines), both for **bright** NEOs with $15 < H < 25$. The shaded areas are 1σ (bold gray), 2σ (medium) and 3σ (light gray) envelopes. We used the best-fit solution (i.e. the one with the maximum likelihood) from the base model and generated 30,000 random samples with 8365 NEOs each (the sample size identical to the number of CSS2's NEOs with $15 < H < 25$). The samples were biased and binned with the standard binning. We identified envelopes containing 68.3% (1σ), 95.5% (2σ) and 99.7% (3σ) of samples and plotted them here. (For interpretation of the references to color in this figure legend, the reader is referred to the web version of this article.)

infer the general characteristics of the faint NEO population from the encounter statistics alone.

We confirm the need for the size-dependent disruption of NEOs at small perihelion distances, as originally pointed out in Granvik et al. (2016) and Paper I. Clearly, any model where the disruption is not taken into account produces a strong excess of low-q (or high-e) orbits. The $q^*(H)$ dependence found here, $q^* = 0.135 + 0.032\,(H - 20)$ with q^* in au, is somewhat steeper – implying disruption at larger perihelion distances for $H > 20$ – than the one inferred in Granvik et al. (2016). Based on this we suggest that small NEOs disrupt at slightly larger perihelion distances than found in Granvik et al. (2016).

5. A case for tidal disruption

We find that the largest excess of CSS NEO detections happens for $1 < a < 1.6$ au, $q \simeq 1$ au and $i \lesssim 10°$ (Fig. 13). In Paper I we tested whether small main-belt asteroids ($D < 100$ m) can drift by the Yarkovsky effect over the ν_6 resonance to directly reach the NEO orbits with $1 < a < 1.6$ au and $e < 0.4$, and found the orbital distribution of NEOs constructed from the simulation with fast drifts was nearly identical to that obtained for the ν_6 resonance with the standard approach. This shows that even very small asteroids cannot pass the ν_6 resonance and the excess of faint NEO detections for $25 < H < 28$ must be related to something else.

Tidal disruption of NEOs is the main suspect (as originally proposed by Granvik and Walsh (2017, 2022, 2023)). The orbits with $1 < a < 1.6$ au, $q \simeq 1$ au and $i \lesssim 10°$ have: (i) large probabilities of having close encounters with the Earth (e.g., Fig. 5 in Morbidelli and Gladman (1998)), and (ii) low encounter speeds ($v_\infty \lesssim 5$ km/s; Fig. 6 in Morbidelli and Gladman (1998)). This is the situation in which tidal disruptions are most likely to happen. For example, Richardson et al. (1998) showed that rubble pile bodies catastrophically disrupt ('Shoemaker-Levy-9' type of disruption) for $v_\infty \lesssim 5$ km/s and encounter distances $d \lesssim 2\ R_{\rm Earth}$, where $R_{\rm Earth} = 6371$ km is the Earth radius. *We therefore propose that the excess of small NEOs identified here ($25 < H < 28$ or $9 < D < 36$ m for the reference albedo $p_V = 0.14$) is caused by tidal disruption of $D \gtrsim 50$ m NEOs.*

A realistic modeling of tidal disruption would require monitoring close planetary encounters of NEOs from each source. Unfortunately, we have not recorded any encounters in the N-body simulations described in Paper I, and we thus cannot conduct a detailed investigation of tidal disruption here. Instead, we performed the following test. NEOMOD works well for $H < 25$ (Fig. 10). We used the base NEOMOD model for $H < 25$ and multiplied the intrinsic NEO population in each

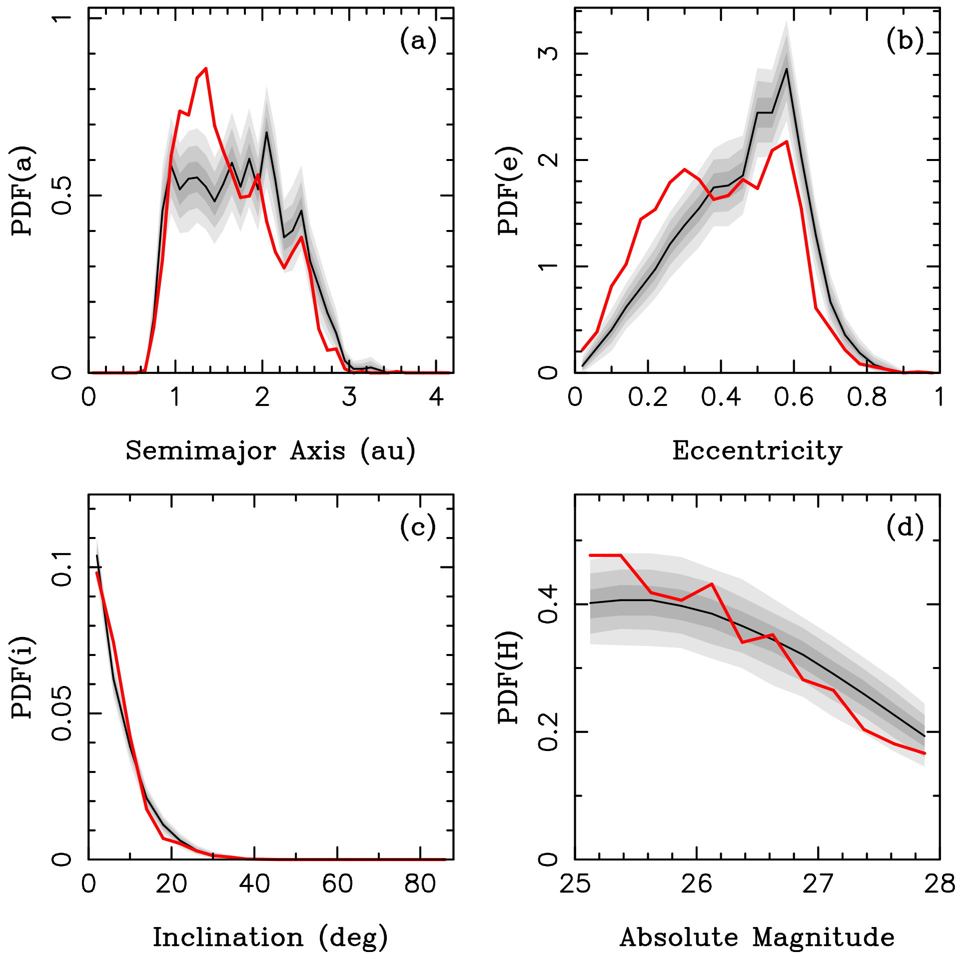

Fig. 11. The probability density functions (PDFs) of a, e, i, and H from our biased base model (black lines) and the CSS2 NEO detections (red lines), both for **faint** NEOs with $25 < H < 28$. The shaded areas are 1σ (bold gray), 2σ (medium) and 3σ (light gray) envelopes. We used the best-fit solution (i.e. the one with the maximum likelihood) from the base model and generated 30,000 random samples with 3003 NEOs each (the sample size identical to the number of CSS2's NEOs with $25 < H < 28$). The samples were biased and binned with the standard binning. We identified envelopes containing 68.3% (1σ), 95.5% (2σ) and 99.7% (3σ) of samples and plotted them here. (For interpretation of the references to color in this figure legend, the reader is referred to the web version of this article.)

orbital bin by the probability that a body in the bin would have a close encounter with the Earth.[16] The probability was computed by the Öpik formalism (Bottke et al., 1994). The resulting orbital distribution, which approximates how fragments of tidally disrupted NEOs would populate orbital space, was normalized to one and supplied to MultiNest as an additional source. Note that this method ignores the orbital evolution of fragments in NEO space. It also assumes that the production of small fragments from tidal disruption is a steady-state process; this would not be quite right if the contribution of only a few random disruption events is important.

We found that including tidal disruption as an additional source does not change the results for bright NEOs ($H < 25$). This is expected because the model without tidal disruption was able to match the orbital and absolute magnitude distribution of bright NEOs (Fig. 10), and the disruption of a few large asteroids is not expected to significantly change the distribution for $H < 25$. For faint NEOs, however, the best fit requires a significant contribution from tidal disruption. Specifically, for $H = 28$, MultiNest estimates the tidal disruption weight $\alpha_{td} = 0.3 \pm 0.05$. The biased best-fit model with tidal disruption is compared to CSS NEO detections in Fig. 14. This plot can be contrasted with Fig. 11 where tidal disruption was ignored. We see that the fit has substantially improved. The excess for $1 < a < 1.6$ au and $e < 0.4$ has nearly disappeared — both the semimajor axis and eccentricity distribution show the overall shapes that match observations much better than in Fig. 11.[17] This suggests that we are on the right track to resolve this problem (Granvik and Walsh, 2017, 2022, 2023). The absolute magnitude distributions of NEOs with and without tidal disruption are practically the same. For example, $\gamma_6 = 0.53 \pm 0.01$ with tidal disruption and $\gamma_6 = 0.509 \pm 0.005$ in the base model without tidal disruption. This means that the magnitude distribution difference for $25 < H < 28$ between HC21 and this work is not resolved when the effects of tidal disruption are (approximately) taken into account. A more realistic modeling of tidal disruption is left for future work.

Accurate modeling of tidal disruption will need to account for the interior structure of NEOs. There is evidence that the interior structure changes for NEOs with $D \simeq 100$ m (roughly $H \simeq 23$). For $D > 100$ m, asteroids do not have – with some exceptions – spins faster

[16] We also built models where the close encounters with Venus and Mars were included, in addition to Earth encounters. The results of these models are very similar to those discussed here for Earth encounters (the Venus-crossing NEO population is relatively small and Mars has a relatively low mass). Here we focus on Earth encounters because the excess of small NEOs happens along the $q \simeq 1$ au line.

[17] The semimajor axis distribution in Fig. 14a can formally be rejected (based on a K–S test), because the biased model distribution is too strongly peaked near 1 au, whereas the CSS detections peak near 1.3 au. Some of our test idealizations can be responsible for this. For example, we adopted a steady state and ignored the orbital evolution of fragments.

Table 2
The median and uncertainties of our base model parameters. The uncertainties reported here were obtained from the posterior distribution produced by MultiNest. They do not account for uncertainties of the CSS detection efficiency. For parameters, for which the posterior distribution peaks near zero, the last column reports the upper limit (68.3% of posteriors fall between zero and that limit).

Label	Parameter	Median	$-\sigma$	$+\sigma$	Limit
α's for $H = 15$					
(1)	ν_6	0.060	0.003	0.003	–
(2)	3:1	0.277	0.028	0.028	–
(3)	5:2	0.073	0.018	0.019	–
(4)	7:3	0.007	0.005	0.007	0.010
(5)	8:3	0.103	0.013	0.013	–
(6)	9:4	0.008	0.005	0.011	0.012
(7)	11:5	0.076	0.014	0.015	–
(8)	2:1	0.039	0.005	0.006	–
(9)	Inner weak	0.183	0.026	0.025	–
(10)	Hungarias	0.063	0.013	0.012	–
(11)	Phocaeas	0.094	0.010	0.010	–
–	JFCs	0.012	0.006	0.007	0.016
α's for $H = 28$					
(12)	ν_6	0.595	0.024	0.022	–
(13)	3:1	0.313	0.020	0.020	–
(14)	5:2	0.019	0.009	0.010	–
(15)	7:3	0.003	0.002	0.004	0.005
(16)	8:3	0.004	0.003	0.006	0.006
(17)	9:4	0.003	0.002	0.004	0.005
(18)	11:5	0.004	0.003	0.006	0.006
(19)	2:1	0.001	0.001	0.002	0.002
(20)	Inner weak	0.008	0.006	0.013	0.014
(21)	Hungarias	0.020	0.014	0.020	0.029
(22)	Phocaeas	0.003	0.002	0.004	0.004
–	JFCs	0.014	0.007	0.008	0.018
H distribution					
(23)	$N_{\rm ref}$	926	29	29	–
(24)	γ_2	0.393	0.013	0.014	–
(25)	γ_3	0.363	0.006	0.006	–
(26)	γ_4	0.313	0.003	0.003	–
(27)	γ_5	0.522	0.006	0.006	–
(28)	γ_6	0.506	0.005	0.005	–
Disruption parameters					
(29)	q_0^*	0.132	0.003	0.002	–
(30)	δq^*	0.031	0.001	0.001	–

than ~10 rotations/day (spin period ~2.5 h). This "spin barrier" most likely indicates that $D > 100$ m asteroids do not have large tensile strength, and are hold together by gravity (Pravec and Harris, 2000). For $D < 100$ m, however, the spins can be as fast as ~1000 rotations per day, indicating that these smaller bodies must often have substantial strength and that their internal structure is probably akin to that of consolidated rock (monolith). This has important implications for tidal disruption. Specifically, the weak NEOs with $D > 100$ m could be relatively easily disrupted during close planetary encounters, whereas the stronger NEOs with $D < 100$ m should survive more often. This could help to explain some of the trends discussed above.

6. Planetary impacts

All planetary impacts were recorded by the N-body integrator (Paper I). The record accounts for impacts of bodies with $q < 1.3$ au (NEOs) and $q > 1.3$ au (e.g., Mars-crossers). We thus have complete information to determine the impact flux on all terrestrial planets, including Mars. We followed 10^5 test bodies from each source and have good statistics to determine the impact flux of NEOs even from distant main belt sources (e.g., 9:4, 2:1). To combine impacts from different sources, we compute the total impact flux, $F_{\rm imp}$, from

$$F_{\rm imp} = n(H) \sum_{j=1}^{n} \alpha_j(H) \frac{p_{{\rm imp},j}(q^*(H))}{\tau_j(q^*(H))} , \tag{12}$$

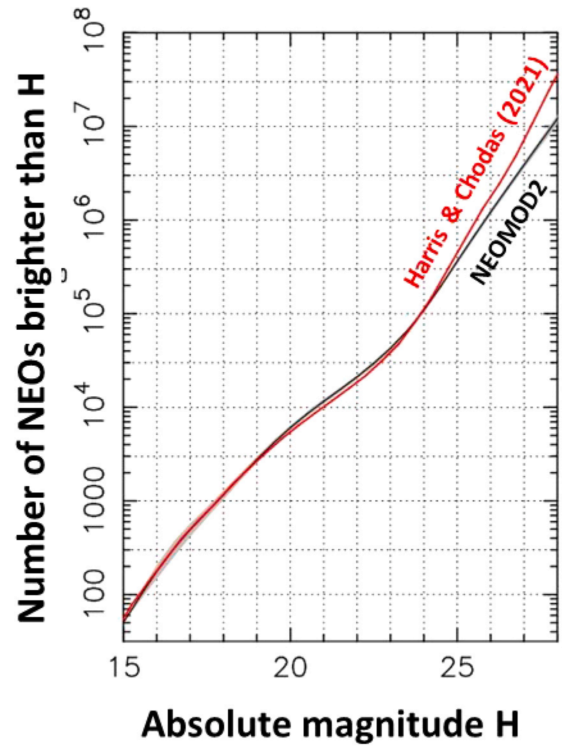

Fig. 12. The intrinsic (debiased) absolute magnitude distribution of NEOs from our base model (black line is the median) is compared to the magnitude distribution from Harris and Chodas (2021) (red line). The gray area is the 3σ envelope obtained from the posterior distribution computed by MultiNest. It contains – by definition – 99.7% of our base model posteriors. (For interpretation of the references to color in this figure legend, the reader is referred to the web version of this article.)

where $n(H)$ is the best-fit absolute magnitude distribution of NEOs, $\alpha_j(H)$ are the magnitude-dependent source weights (Table 2), $p_{{\rm imp},j}$ is the probability of planetary impact for each body inserted in the source j, and τ_j is the mean lifetime of NEOs evolving from the source j. Parameters $p_{{\rm imp},j}$ and τ_j depend on q^* and are therefore also a function of H (via the linear relationship between q^* and H, as defined by the best-fit model). We reported them for a reference value $q^* = 0.1$ au in Table 5 in Paper I.

Fig. 15 shows $F_{\rm imp}(H)$, converted to a cumulative distribution, for the terrestrial planets. For comparison, we also plot the impact flux on the Earth from HC21 who estimated it by multiplying their absolute magnitude distribution $n(H)$ (illustrated in Fig. 12) by a constant (i.e., magnitude independent) impact probability $P_{\rm i} = 1.5 \times 10^{-3}$ Myr^{-1} (Stuart, 2001; Harris and D'Abramo, 2015). We confirmed in Paper I that this is a correct assumption for large NEOs ($H \lesssim 20$), and only for large NEOs (see below). Consistently with Paper I, here we find that the average interval between impacts of $H < 17.75$ NEOs ($D > 1$ km for $p_{\rm V} = 0.14$) is 650 kyr. Applying the same fixed impact probability to small NEOs, HC21 found that the average interval between impacts of $H < 28$ NEOs (roughly $D > 10$ m for $p_{\rm V} = 0.14$) is ≃19 yr. In Paper I, we already explained that the impact probability changes with absolute magnitude; this happens because the ν_6 resonance – known for its high impact probability (Table 5 in Paper I) – is an important source of small NEOs. In the case without tidal disruption, here we find $P_{\rm i} = 2.9 \times 10^{-3}$ Myr^{-1} for $H = 28$ (nearly two times the nominal) and the average interval between impacts ≃29 yr (HC21 population is ≃3 times higher for $H < 28$ but the impact probability is ≃2 times lower). With tidal disruption, the average interval between impacts of $H < 28$ NEOs is ≃17 yr.

Table 3
The absolute magnitude distribution and completeness of the NEO population. The columns are: the lower limit of a magnitude bin (H_1), upper limit of a magnitude bin (H_2), NEOMOD estimate of the number of NEOs between H_1 and H_2 (dN), NEOMOD estimate of the number of NEOs with $H < H_2$ ($N(H_2)$), Harris and Chodas (2021) estimate of $N(H_2)$ ($N_{\rm HC}(H_2)$), NEOMOD estimate of $N(H_2)$ minus 1σ ($N_{\rm min}(H_2)$), NEOMOD estimate of $N(H_2)$ plus 1σ ($N_{\rm max}(H_2)$), number of NEOs with $H < H_2$ in the MPC catalog from October 2022 ($N_{\rm MPC}(H_2)$), completeness defined as $N_{\rm MPC}(H_2)/N(H_2)$, and 1σ completeness range (<1% uncertainties not listed).

H_1	H_2	dN	$N(H_2)$	$N_{\rm HC}(H_2)$	$N_{\rm min}(H_2)$	$N_{\rm max}(H_2)$	$N_{\rm MPC}(H_2)$	Compl.	Range
15.25	15.75	61.2	130	136	124	137	123	95%	(90–99)
15.75	16.25	104	234	235	219	250	210	90%	(84–96)
16.25	16.75	156	390	398	365	416	361	93%	(87–99)
16.75	17.25	218	608	621	579	639	562	92%	(88–97)
17.25	17.75	328	936	940	898	977	854	91%	(87–95)
17.75	18.25	513	0.145E4	0.147E4	0.140E4	0.151E4	1 325	91%	(88–95)
18.25	18.75	790	0.224E4	0.221E4	0.217E4	0.232E4	2 022	90%	(87–93)
18.75	19.25	0.117E4	0.341E4	0.323E4	0.331E4	0.350E4	2 897	85%	(83–88)
19.25	19.75	0.164E4	0.505E4	0.463E4	0.492E4	0.517E4	4 021	80%	(78–82)
19.75	20.25	0.216E4	0.721E4	0.642E4	0.703E4	0.737E4	5 281	73%	(72–75)
20.25	20.75	0.272E4	0.992E4	0.873E4	0.970E4	0.101E5	6 636	67%	(66–68)
20.75	21.25	0.350E4	0.134E5	0.118E5	0.131E5	0.137E5	8 076	60%	(59–60)
21.25	21.75	0.471E4	0.181E5	0.159E5	0.178E5	0.185E5	9 480	52%	(51–53)
21.75	22.25	0.673E4	0.249E5	0.217E5	0.244E5	0.254E5	10 865	44%	(43–45)
22.25	22.75	0.104E5	0.353E5	0.314E5	0.345E5	0.360E5	12 309	35%	(34–36)
22.75	23.25	0.173E5	0.525E5	0.476E5	0.514E5	0.536E5	13 862	26%	–
23.25	23.75	0.311E5	0.836E5	0.826E5	0.818E5	0.853E5	15 673	19%	–
23.75	24.25	0.608E5	0.144E6	0.153E6	0.142E6	0.147E6	17 622	12%	–
24.25	24.75	0.121E6	0.266E6	0.313E6	0.260E6	0.272E6	19 709	7.4%	–
24.75	25.25	0.229E6	0.494E6	0.641E6	0.482E6	0.506E6	21 724	4.4%	–
25.25	25.75	0.411E6	0.905E6	0.130E7	0.882E6	0.928E6	23 636	2.6%	–
25.75	26.25	0.728E6	0.163E7	0.241E7	0.159E7	0.168E7	25 337	1.6%	–
26.25	26.75	0.129E7	0.292E7	0.481E7	0.284E7	0.300E7	26 728	0.9%	–
26.75	27.25	0.225E7	0.517E7	0.108E8	0.500E7	0.534E7	27 849	0.5%	–
27.25	27.75	0.395E7	0.912E7	0.244E8	0.875E7	0.949E7	28 653	0.3%	–

An interesting difference between HC21 and this work is identified for intermediate-size NEOs ($20 < H < 26$; Fig. 15). For example, HC21 estimated that the mean time between impacts of $H < 22$ NEOs ($D >$ 140 m for the reference albedo $p_{\rm V} = 0.14$) is ≃37,000 yr, whereas we find ≃21,400 yr. This is contributed by two factors: (1) our population of $H < 22$ NEOs is slightly larger that the one reported in HC21 (Fig. 12), and (2) our impact probability for $H < 22$ NEOs is slightly higher ($P_{\rm i} = 2.4\times10^{-3}$ Myr^{-1} for $H = 22$; due to the larger contribution of the ν_6 resonance to small NEOs). Using our estimate and assuming the Poisson statistics, the probability of one impact of a $H < 22$ NEO on the Earth in the next 1000 yr is found to be ≃4.5%.

7. Discussion

7.1. Terrestrial impacts of small NEOs

Brown et al. (2002) analyzed satellite records of bolide detonations in the Earth's atmosphere to estimate the impact flux of ∼1–10 m bodies. For $D \simeq 10$ m, roughly equivalent to $H = 28$ for our reference albedo $p_{\rm V} = 0.14$, the average interval between impacts was found ≃10 yr (with a factor of ≃2 uncertainty). The infrasound data from Silber et al. (2009), as reported by Brown et al. (2013), indicate a somewhat shorter interval but the error bars of these estimates overlap with the bolide data. As for fireball events recorded on the CNEOS website,[18] at least three impactors over the past 20 yr, including the Chelyabinsk meteorite (Brown et al., 2013), had estimated pre-atmospheric-entry diameters $D > 10$ m. Together, these estimates suggest that the average interval between $D > 10$ m impacts is ≃10 yr, or perhaps even somewhat shorter.

These results motivated HC21 to use a slightly steeper extrapolation of the NEO magnitude distribution to $H \sim 28$ such that their impact flux estimate is more in line with impact observations. Here we showed that the magnitude distribution is in fact relatively shallow ($\gamma \simeq 0.51$ for $15 < H < 28$) but the impact probability on the Earth increases for smaller NEOs (due to preferential sampling of the ν_6 resonance and tidal disruption). The mean interval between impacts of $H < 28$ NEOs is estimated here to be ≃17 yr (Fig. 15). This is a factor of $\gtrsim 1.7$ longer than the estimates based on bolides, infrasound and CNEOS. We speculate that the effects of tidal disruption may be even more important for terrestrial impacts than our simple test in Section 5 would indicate. A detailed investigation of tidal disruption is left for future work.

7.2. Lunar/martian craters

Our work could explain the difference between the size distributions of lunar and Martian craters (Daubar et al., 2022). The recently formed, small Martian craters have relatively shallow size distribution (≃2.2 cumulative index from Daubar et al. (2022)). For small lunar craters, Neukum et al. (2001) reported ≃3.4 cumulative index for crater diameters ≃0.1–2 km, which would correspond to ≃3–100 m impactors (the distribution is probably even steeper for smaller impactors; (Speyerer et al., 2020)). The size distribution of small lunar craters is thus significantly steeper than the size distribution of small Martian craters. Previous work sought to explain this difference by meteoroid ablation and fragmentation in Martian atmosphere (Popova et al., 2003), but the atmospheric effect should be irrelevant for $D > 10$ m impactors. Secondary impacts, which can contribute to the size distribution of small craters, should have similar effects for the Moon and Mars. As an important caveat, we note that the craters reported in Daubar et al. (2022) are very small, roughly corresponding to $D < 10$ m impactors.

Here we find the cumulative index ≃3.1 for small lunar impactors and ≃2.5 for small Martian impactors ($25 < H < 28$ or $9 < D < 36$ m for $p_{\rm V} = 0.14$). The lunar distribution is steeper for two reasons: (1) Small NEOs preferentially evolve from the ν_6 resonance; this favors lunar impacts because small objects spend shorter time on Mars-crossing orbits than the large ones (their impact window is short). (2) Tidal disruption produces excess of small NEOs ($25 < H < 28$) for $1 < a < 1.6$ au, $q \simeq 1$ au and $i \lesssim 10°$ (Section 5), and these fragments are more likely to hit the Moon (or Earth) than Mars. Tidal disruption during close encounters to Mars should happen as well but it is hard to find

[18] https://cneos.jpl.nasa.gov/fireballs/.

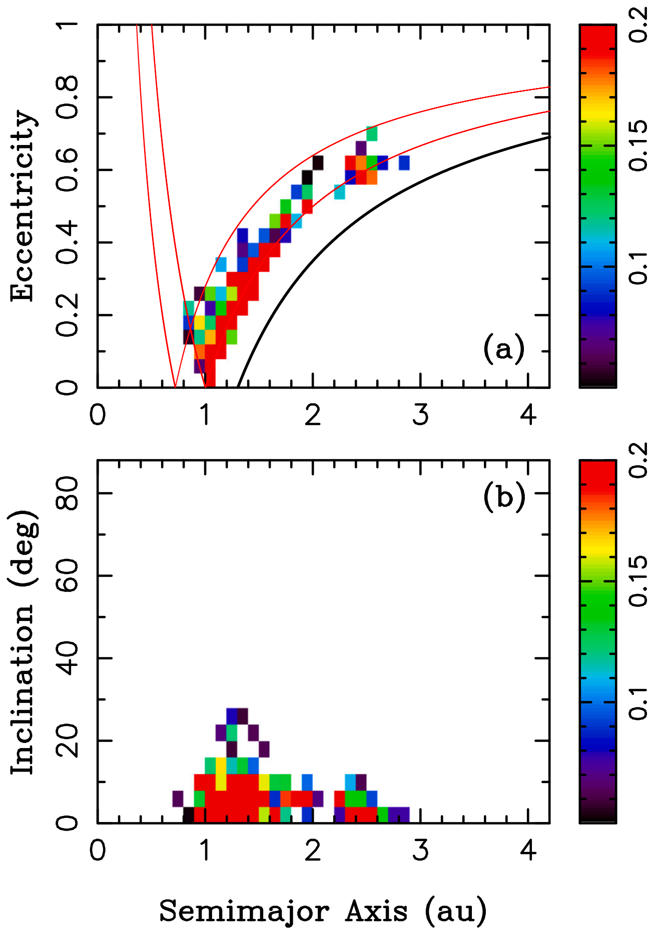

Fig. 13. The excess of $25 < H < 28$ NEOs detected by new CSS relative to our base model for $25 < H < 28$ (Section 4). We binned NEOs detected by CSS2 with the standard binning (Paper I), subtracted the number of NEOs predicted in each bin by our biased best fit model, $\mathcal{M}_b$, and normalized it by $\mathcal{M}_b$. The red color shows that the largest excess, roughly 20%–30%, happens for $1 < a < 1.6$ au, $q \simeq 1$ au and $i \lesssim 10°$. The red lines show borders of the orbital domain where orbits can have close encounters with Earth and Venus. The black line corresponds to $q = 1.3$ au. (For interpretation of the references to color in this figure legend, the reader is referred to the web version of this article.)

any evidence for that in the CSS data (this may suggest that no large tidal disruption events happened during Mars encounters recently).[19]

For $H \sim 28$, the Mars-to-Moon impact ratio, normalized to the unit surface area, is found to be $R_b = 0.8$ in the model without tidal disruption and $R_b = 0.5$ in the model with tidal disruption. The trend of decreasing R_b for smaller impactors is consistent with the results reported in Paper I, where we found $R_b = 1.2$ for $H \sim 25$. For reference, Hartmann (2005) and Marchi (2021) adopted $R_b = 2.6$ for all asteroid impactor sizes when they used the lunar chronology for Mars. With our new R_b estimates, which imply lower impact flux on Mars, the young terrains on Mars dated from $9 < D < 36$ m impacts should be ∼2–5 times older than thought before.

7.3. PM excess of meteorite falls

Tidal disruption could also help to explain the PM excess of meteorite falls (Paper I). The PM/AM ratio measures the relative frequency of meteorite falls before (6–12 h) and after (12–18 h) noon. It is usually reported as the number of afternoon falls (12–18 h) over the number of day-time falls (6–18 h), to express the observed excess of afternoon falls, here denoted as $\mathcal{E}$. Ordinary chondrites (OCs), for example, have $\mathcal{E} = 0.63 \pm 0.02$ (Wisdom, 2017), but in Paper I we obtained $\mathcal{E} = 0.47 \pm 0.02$ and 0.50 ± 0.05 for the ν_6 and 3:1 resonances, respectively (also see Morbidelli and Gladman (1998)). This difference could be resolved because the excess small NEOs detected by CSS, which we attribute to tidal disruption here, happens for $1 < a < 1.6$ au, $q \simeq 1$ au and $i \lesssim 10°$, and impacts from these orbits are expected to have $\mathcal{E} > 0.6$ (Fig. 6 in Morbidelli and Gladman (1998)). We leave a detailed investigation of this issue for future work.

7.4. Orbits and CRE ages of meteorites

Our work suggests that tidal disruption should be progressively more important for small terrestrial impactors and if so, we would expect that many meteorites should have orbits with $1 < a < 1.6$ au and $q \simeq 1$ au. But this does not seem to be the case: the meteorite falls and bolides detected by US Government sensors show a broad orbital range with $q = a(1-e) < 1$ au and $Q = a(1+e) > 1$ au (Brown et al., 2013, 2016; Granvik and Brown, 2018). It could be that some additional dependencies make a difference. For example, the bolide detections should scale with the kinetic energy of the impactor. This means that disrupted objects, which have relatively low impact speeds and thus lower impact energies, should have a reduced presence the detected bolide flux. When we fold this dependence into the orbital distribution of small impactors, we find that the orbital distribution of bolides from the model is actually consistent with bolide observations.[20]

It needs to be emphasized that the pre-atmospheric-entry diameters of meteorites are characteristically ∼0.1 m, which is a factor of ∼100 in size below where we constrained NEOMOD2 from the telescopic observations of NEOs ($D \gtrsim 10$ m). The impactor sizes reported from US Government sensors are typically ∼1 m (Brown et al., 2016). So, there could also be something problematic with extrapolating our expectations from $D \gtrsim 10$ m to $D \lesssim 1$ m.

In addition, if many small NEOs were produced in relatively recent tidal disruption events of larger NEOs, we would expect that many meteorites would have short Cosmic Ray Exposure (CRE) ages. But the CRE distribution of ordinary chondrites does not seem to require any recent tidal disruption events (Vokrouhlický and Farinella, 2000; except, perhaps, for the CRE peak of H chondrites at 7–8 Myr). It may be the case that tidal disruption affects carbonaceous (C-type) NEOs to a larger degree, because they are weaker and have lower density than ordinary chondrites. Noble gas analysis has indicated that the CRE ages of most CM and CI chondrites are 0.1–1 Myr, significantly younger than ages of other carbonaceous and ordinary chondrites (1–100 Myr; Eugster et al., 2006). Krietsch et al. (2021) found that the main CRE age cluster of CMs is at ≃0.2 Myr and observed further minor peaks at 1, 4.5–6, and 8 Myr.

7.5. Observational completeness

The last two columns in Table 3 show the NEOMOD2 prediction for the observational completeness of NEOs. To use the same magnitude system from which NEOMOD2 was derived, completeness is reported relative to the MPC catalog from October 2022 (this defines the absolute magnitude system used in this is work). The more recent MPC catalogs are (slightly) more complete as they include new NEO discoveries since October 2022. Unfortunately, we cannot rigorously use these catalogs because the absolute magnitudes reported for many NEOs and MBAs, for which we derived the CSS detection efficiencies,

[19] Alternatively, small NEOs produced by tidal encounters to Mars do become bright enough, given their relatively distant orbits, to be detected by a terrestrial observer.

[20] The statistics is not ideal because (Brown et al., 2016) only reported ∼50 bolide orbits; additional detection biases can also be an issue.

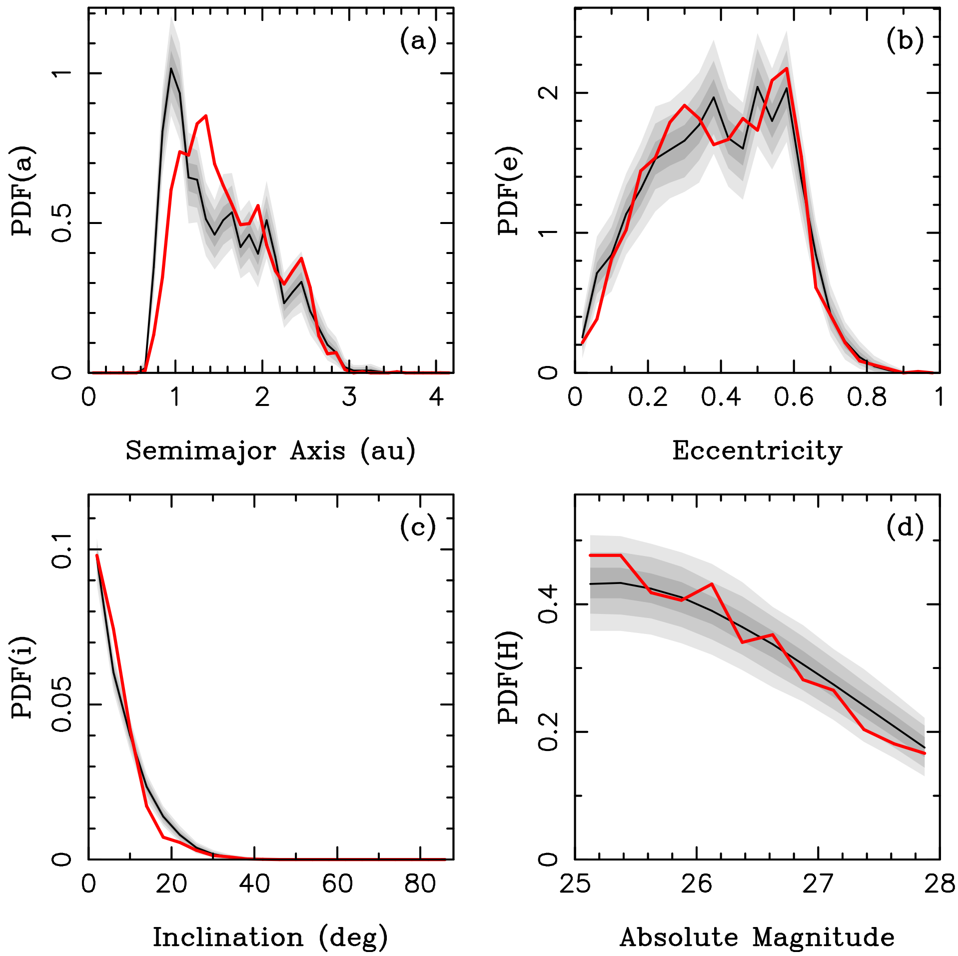

Fig. 14. The probability density functions (PDFs) of a, e, i, and H from our biased based model with tidal disruption (black lines) and the CSS2 NEO detections (red lines), both for faint NEOs with $25 < H < 28$. The shaded areas are 1σ (bold gray), 2σ (medium) and 3σ (light gray) envelopes. We used the best-fit solution (i.e. the one with the maximum likelihood) from the model with tidal disruption and generated 30,000 random samples with 3003 NEOs each (the sample size identical to the number of CSS2's NEOs with $25 < H < 28$). The samples were biased and binned with the standard binning. We identified envelopes containing 68.3% (1σ), 95.5% (2σ) and 99.7% (3σ) of samples and plotted them here. (For interpretation of the references to color in this figure legend, the reader is referred to the web version of this article.)

have changed: the H magnitudes became on average fainter by a fraction of mag (Pravec et al., 2012). The shifting magnitudes mean that the actual number of NEOs brighter than H (or larger than D) is lower ($N(H_2)$ values in Table 3 should be lower) than what we have inferred from the MPC catalog released in October 2022.[21] This issue, in itself, should not affect the completeness of the population reported in Table 3 (assuming that NEOs and main belt asteroids are similarly affected). To rigorously test this, the magnitude system of NEOMOD would have to be updated to the new magnitudes, and this would essentially require to repeat many steps described in Sections 2 and 3. We leave this for future updates. To approximately align the estimated NEO population in this work with new MPC magnitudes, one can compare the number of known NEOs in Table 3 ($N_{\rm MPC}(H_2)$) with the number of known NEOs with $H < H_2$ in any new catalog, defining the ratio $f = N_{\rm MPC,new}(H_2)/N_{\rm MPC}(H_2)$, and apply it as a multiplication factor to the NEOMOD estimate in Table 3 ($N(H_2)$), obtaining $N(H_2)_{\rm new} = f \times N(H_2)$. For example, if $f = 805/854 = 0.943$ for $H < 17.75$ (Table 3 and MPC catalog from March 2023; Harris and Chodas, 2023), then $N_{\rm new}(17.75) \simeq 0.943 \times 936 = 882$.

The results reported in Table 3 indicate that the population of small NEOs is largely incomplete (Fig. 16). For example, we find that the completeness for $H < 22.75$ ($D > 100$ m for $p_V = 0.14$) is $\simeq$26%. This compares reasonably well with HC21 who found a $\simeq$34% completeness for $H < 22.75$ (Harris and Chodas, 2023 estimated a $\simeq$40% completeness for $H < 22.75$). Our results start to diverge from HC21 and Harris and Chodas (2023) for smaller NEOs. For the faintest magnitudes considered in our work, we find a $\simeq$0.3% completeness for $H < 27.75$, whereas HC21 and Harris and Chodas (2023) reported only a $\simeq$0.09% completeness for $H < 27.75$. These differences are ultimately driven by the shallower absolute magnitude distribution that we obtain here for $H > 25$ (Fig. 12 and Section 4).

Interestingly, the NEOMOD2 results suggest that even the population of bright NEOs could be significantly incomplete. For example, the estimated completeness for $H < 17.75$ is 91 ± 4% (note that this is the completeness of the MPC catalog released in October 2022; the H magnitudes updates in the new catalogs complicate things). This would imply that 44–123 $H < 17.75$ NEOs have yet to be discovered. The formal uncertainty of our estimate is relatively large. For comparison, HC21 and Harris and Chodas (2023) used the redetection method to estimate the completeness of $H < 17.75$ NEOs at $\simeq$96%, which is just about one sigma above our estimate. The redetection method may

[21] For example, Harris and Chodas (2021) had 898 known NEOs with $H < 17.75$ (MPC catalog from August 8, 2020), we have 854 known NEOs with $H < 17.75$ (MPC catalog from October 19, 2022), and Harris and Chodas (2023) have 805 known NEOs with $H < 17.75$ (MPC catalog from March 13, 2023). As no individual asteroids were dropped from the MPC catalog, this means that nearly one hundred NEOs with estimated $H < 17.75$ in 2020 now have $H > 17.75$. This is a dramatic shift.

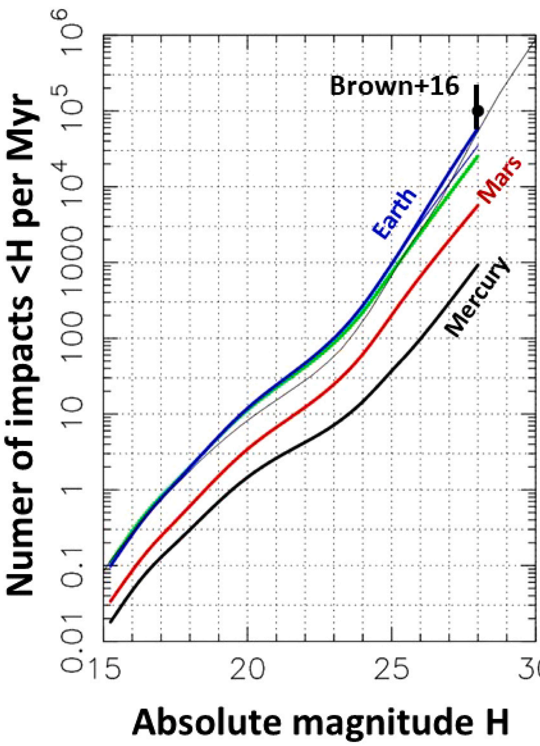

Fig. 15. The impact flux on the terrestrial planets for our base model with tidal disruption. The black, green, blue and red lines show the impact flux for Mercury, Venus, Earth and Mars from Eq. (12). With a 30% contribution of tidal disruptions at $H = 28$, the mean time between impacts of $D > 10$ m NEOs is ≃17 years (was ≃30 years in the base model without tidal disruption; thin blue line), which is more consistent with bolide and infrasound observations (Brown et al., 2002, 2013; black dot). The thin black line is the NEO magnitude distribution from Harris and Chodas (2021) scaled with the fixed impact probability (1.5×10^{-3} Myr^{-1}; see the main text). (For interpretation of the references to color in this figure legend, the reader is referred to the web version of this article.)

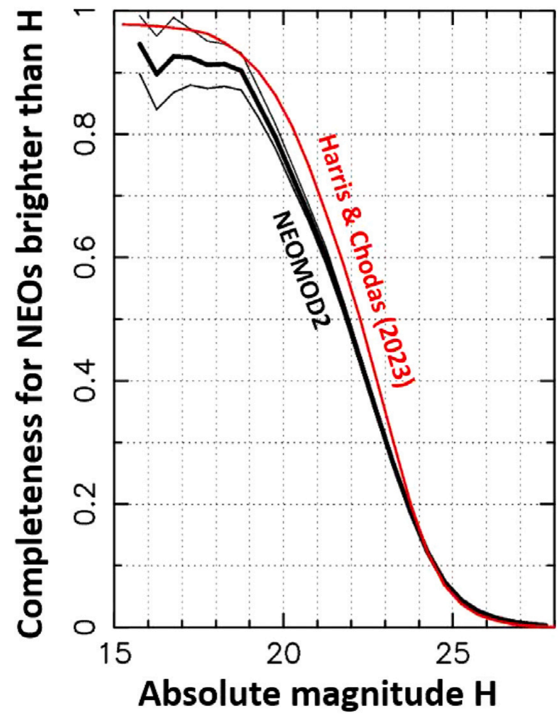

Fig. 16. The estimated completeness of the NEO population from our base model (thick black line; the two thin lines show 1 sigma uncertainty; Table 3) is compared to the completeness estimated in Harris and Chodas (2023) (red line). For $H < 19$, the completeness given in Harris and Chodas (2023) is consistent with 1 sigma envelope of our results. The redetection method may provide a more accurate completeness estimate for these bright NEOs. Our model indicates slightly lower completeness than Harris and Chodas (2023) for $19 < H < 24$, and slightly higher completeness than Harris and Chodas (2023) for $H > 24$. (For interpretation of the references to color in this figure legend, the reader is referred to the web version of this article.)

provide a more accurate completeness estimate for these bright NEOs for which the redetection statistics is good. Related to that, it would be worthwhile to quantify various uncertainties of the redetection method and their impact on the completeness estimate. Seven $H < 17.75$ NEOs were discovered in the past two years (2022–2023): 2022 KL8, 2023 HQ2, 2022 AP7, 2023 PS2, 2022 QK204, 2023 GZ1, and 2022 RX3. Many of these have large inclinations (five have $i > 30°$) and/or large semimajor axes (five have $a > 2.8$ au). At this rate, it could take over a decade to find 99% of all $H < 17.75$ NEOs ($a < 4.2$ au).

To understand where the bright NEOs may be hiding, we generated a large sample of bright NEOs from the NEOMOD Simulator and ran them through the CSS detection pipeline. We used the G96 observations from 2005–2022 and 703 observations from 2005–2012. This cumulatively corresponds to 28 years of NEO observations from the northern hemisphere. We found that ≃4% of bright NEOs do not appear in any frame taken by CSS and would thus avoid detection. Most of these objects have $a \lesssim 1.2$ au and avoid detection due to the synodic effect, or have the argument of perihelion $\omega \sim 90°$ — and therefore appear in the southern hemisphere near opposition. Two ATLAS NEO-survey telescopes with large FoVs just started operations from the southern hemisphere (Chile and Southern Africa). By simulating their detection capabilities (Deienno et al., 2023), we find that both of these telescopes should be very effective in detecting bright NEOs that escape detections from the northern hemisphere. Indeed, W68 (Chile) has recently a discovery of 2022 RX3, a potentially hazardous NEO with $H = 17.7$.

7.6. Collisional evolution of small NEOs

We used the Öpik formalism (Bottke et al., 1994) to estimate the collisional probabilities and velocities among NEOs, and between NEOs and main belt asteroids (MBAs). The intrinsic probability for collisions among NEOs is relatively high, $P_{\rm i} \simeq 6.5 \times 10^{-18}$ km^{-2} yr^{-1}, but the population of NEOs is much smaller than MBAs; collisions among NEOs can therefore be neglected. The probabilities and velocities for collisions between NEOs and MBAs are $P_{\rm i} \simeq 2.6 \times 10^{-18}$ km^{-2} yr^{-1} and $V_{\rm i} \simeq 11.6$ km/s. The impact speeds are therefore ≃2 times higher than in the case of collisions among MBAs. Taking this into account we estimate that the collisional lifetime of NEOs should be ∼3 times shorter, on average, than the collisional lifetime of MBAs. For MBAs, Bottke et al. (2005) reported that the average collisional lifetime is ∼30 Myr for $D \simeq 10$ m. This allows us to estimate that the collisional lifetime of $D \simeq 10$ m NEOs is ∼10 Myr, only slightly longer than the dynamical lifetime of NEOs produced from the ν_6 resonance (Table 5 in Paper I; other resonances give much shorter dynamical lifetimes). This means that it may be justified, but barely so, to neglect the collisional evolution of NEOs for $D > 10$ m. Conversely, for $D < 10$ m, the collisional lifetime of NEOs would have to be taken into account. For reference, here we estimate that the average collisional lifetime of $D \simeq 1$ m NEO is ∼5 Myr.

7.7. Distribution of NEO obliquities

La Spina et al. (2004) reported a ∼2:1 preference for retrograde rotation among large NEOs ($D \gtrsim 1$ km). They interpreted this result in the context of the NEO model from Bottke et al. (2002). In the Bottke et al. model, the ν_6 resonance contributes to ≃37% of NEOs.

To reach ν_6, a main belt asteroid must have a retrograde rotation and drift inward; this implies that the ν_6 resonance should produce predominantly retrograde NEOs. Other important sources of NEOs, including the 3:1 resonance and weak resonances in the inner belt, can be reached from both sides, and this implies that they should be producing and roughly equal share of prograde and retrograde NEOs. La Spina et al. (2004) therefore found from this argument that the ratio of retrograde to prograde NEOs should be $(37 + 63/2)$: $63/2$ or ∼2:1, in good agreement with observations.

NEOMOD2 indicates a much smaller contribution of ν_6 resonance to large NEOs: $\alpha_{\nu 6} = 0.06 \pm 0.03$ for $H \simeq 15$. If this is correct, the contribution of the ν_6 resonance to large retrograde NEOs would be minimal. We therefore suggest that the preference for retrograde rotation of large NEOs is probably related to something else. There are at least two possibilities:

(1) We find that the number of $H < 18$ MBAs on the sunward side of the 3:1 resonance is significantly lower (by ∼50%) than on the opposite side. This asymmetry, which favors generation of retrograde NEOs from 3:1, is contributed by asteroid families (Nesvorný et al., 2015).

(2) Ďurech and Hanuš (2023) obtained the distribution of $D > 1$ km MBAs from a Gaia-DR3 data analysis (Gaia Collaboration et al., 2023). They showed that retrograde MBAs often have the obliquity $\theta \simeq 180°$, most likely because they reached the terminal state of the YORP evolution (Vokrouhlický et al., 2015). The prograde MBAs, however, show a broader distribution of obliquities (roughly $0 < \theta \lesssim 60°$). This presumably happens because prograde rotators can be captured in spin–orbit resonances that can prevent them from reaching $\theta \simeq 0$ (Vokrouhlický et al., 2003). All this means that the retrograde MBAs should have, on average, faster Yarkovsky drift rates (the Yarkovsky drift rate scales with $\cos\theta$; Vokrouhlický et al. (2015)) than prograde MBAs; they more likely reach resonances and evolve onto NEO orbits.[22]

Asymmetric feeding of the 3:1 and other strong resonances could provide a possible explanation for the preference for retrograde rotation among large NEOs (La Spina et al., 2004). Farnocchia et al. (2013) analyzed obliquities of small, sub-km NEOs and found that $81 \pm 8\%$ have retrograde rotation (i.e., roughly a 4:1 preference for retrograde rotation). The increasing share of retrograde rotators among smaller NEO is likely related the fact that the ν_6 resonance contribution to the NEO population increases for small bodies. For example, for $D \simeq 0.1$ km ($H \simeq 22.75$ for $p_V = 0.14$), the ν_6 contribution is ≃40%, which is already similar to the ν_6 contribution adopted in La Spina et al. (2004). This presumably could, when combined with obliquity distribution differences discussed above, explain the 4:1 preference for retrograde rotation among small NEOs (Farnocchia et al., 2013).

8. Summary

The main results of this work are summarized as follows.

(1) We updated the previous NEO model. NEOMOD v2.0 is based on numerical integrations of bodies from 12 sources (11 main-belt sources and comets). A flexible method to accurately calculate biases of NEO surveys was applied to the Catalina Sky Survey (CSS) observations from 2013 to 2022, when CSS detected ≃14,000 unique NEOs (this can be compared to only ≃4500 unique NEOs detected by CSS from 2005 to 2012 (Paper I, Granvik et al., 2018). The `MultiNest` code (Feroz and Hobson, 2008; Feroz et al., 2009) was used to optimize the model fit to CSS detections.

(2) The best-fit orbital and absolute magnitude NEO model is available via the NEOMOD Simulator,[23] a code that can be used to generate user-defined NEO samples from the model. Researchers interested in the probability that a specific NEO evolved from a particular source can obtain this information from the ASCII table that is available along with the Simulator.

(3) We confirm that the sampling of main-belt sources by NEOs is *size-dependent* with the ν_6 and 3:1 resonances contributing ∼30% of NEOs with $H \sim 15$, and ∼90% of NEOs with $H \sim 28$. This trend most likely arises from how the small and large main-belt asteroids reach the source regions. We confirm the size-dependent disruption of NEOs reported in Granvik et al. (2016) and Paper I. As a consequence of the size-dependent sampling and disruption, small and large NEOs have different orbital distributions.

(4) We found a shallower absolute magnitude distribution for $25 < H < 28$ and smaller number of NEOs with $H < 28$ than Harris and Chodas (2021). This may point to some problem with the detection efficiency of CSS. Alternatively, some of the assumptions in Harris and Chodas (2021) may not be quite right. When tidal disruption is ignored, the average time between terrestrial impacts of $D > 10$ m bolides is found here to be 29 yr — ≃1.5 and ≃3 times longer than the nominal estimates from Harris and Chodas (2021) and Brown et al. (2002, 2013). See item (6) below for the results with tidal disruption.

(5) We estimate 936 ± 29 NEOs with $H < 17.75$ ($D > 1$ km for $p_V = 0.14$) and $a < 4.2$ au. With 854 known $H < 17.75$ NEOs (as of October 2022), the NEO population with $H < 17.75$ is 87%–95% complete (1σ interval). Many of the yet-to-be-detected bright NEOs should have large orbital inclinations and/or large semimajor axes. The hemispheric bias will be reduced as two ATLAS telescopes continue to operate from the south hemisphere. The known NEO population with $H < 22$ ($D > 140$ m for $p_V = 0.14$) is only 47%–49% complete.

(6) The excess of CSS NEO detections for $1 < a < 1.6$ au, $q \simeq 1$ au, $i \lesssim 10°$ and $25 < H < 28$ (Figs. 11 and 13) is attributed to tidal disruption of larger NEOs during close encounters with the Earth. The orbital fit significantly improves in a model where tidal disruption is (approximately) accounted for. With tidal disruption, the average time between terrestrial impacts of $D > 10$ m bolides is found to be ≃17 yr. Tidal disruption could also help to explain the PM excess of meteorite falls and differences in lunar and Martian crater size distributions.

(7) For $H \sim 28$, the Mars-to-Moon impact ratio, normalized to the unit surface area, is found to be $R_b = 0.8$ in the model without tidal disruption and $R_b = 0.5$ in the model with tidal disruption. Previous works used $R_b = 2.6$ for all asteroid impactor sizes (Hartmann, 2005; Marchi, 2021) to apply the lunar crater chronology to Mars; this may be incorrect, especially for small impactors. The trend of decreasing R_b for smaller impactors is consistent with the results reported in Paper I, where we found $R_b = 1.2$ for $H \sim 25$.

(8) We suggest that the distribution of obliquities of large NEOs, which shows a ∼2:1 preference for retrograde rotation (La Spina et al., 2004), may be related to (on average) faster Yarkovsky drift rates of retrograde main belt asteroids (given that their obliquities are more tightly clumped near 180°, Ďurech and Hanuš (2023); Sect. 7.7), and/or to the asymmetric distribution of main belt asteroids around source resonances (e.g., 3:1; Section 7.7). The larger share of retrograde rotators among smaller NEOs (Farnocchia et al., 2013) is likely related the fact that the ν_6 resonance contribution increases for small NEOs (the ν_6 resonance can only be reached by sunward-drifting bodies with $\theta > 90°$).

[22] It needs to be demonstrated whether the asymmetric feeding of resonances by faster drifting retrograde MBAs can remain in a steady state. Without a distant source, the retrograde MBAs on the outer side of the 3:1 resonance ($a > 2.5$ au) would end up evolving into the resonance. Their number density in a narrow strip near the 3:1 resonance would decrease, and this would affect the feeding rate. In reality, however, the number density of MBAs on the outer side of the 3:1 resonance is larger than on the sunward side (see item (1) above).

[23] https://www.boulder.swri.edu/~davidn/NEOMOD_Simulator and GitHub.

(9) The impact probability of a $H < 22$ ($D > 140$ m for $p_V = 0.14$) object on the Earth in this millennium is estimated to be ≃4.5%.

Declaration of competing interest

The authors declare that they have no known competing financial interests or personal relationships that could have appeared to influence the work reported in this paper.

Data availability

Data will be made available on request.

Acknowledgments

The simulations were performed on the NASA Pleiades Supercomputer. We thank the NASA NAS computing division for continued support. The work of DN, RD, WFB and DF was supported by the NASA Planetary Defense Coordination Office project "Constructing a New Model of the Near-Earth Object Population". The work of SN, SRC, PWC and DF was conducted at the Jet Propulsion Laboratory, California Institute of Technology, under a contract with the National Aeronautics and Space Administration. DV acknowledges support from the grant 21-11058S of the Czech Science Foundation. We thank Alan Harris and the anonymous reviewer for helpful comments. Alan Harris graciously provided data from Harris and Chodas (2023) for Fig. 16.

References

Bottke, W.F., Nolan, M.C., Greenberg, R., Kolvoord, R.A., 1994. Velocity distributions among colliding asteroids. Icarus 107, 255–268. http://dx.doi.org/10.1006/icar.1994.1021.

Bottke, W.F., et al., 2002. Debiased orbital and absolute magnitude distribution of the near-earth objects. Icarus 156, 399–433. http://dx.doi.org/10.1006/icar.2001.6788.

Bottke, W.F., et al., 2005. Linking the collisional history of the main asteroid belt to its dynamical excitation and depletion. Icarus 179, 63–94. http://dx.doi.org/10.1016/j.icarus.2005.05.017.

Bowell, E., Hapke, B., Domingue, D., Lumme, K., Peltoniemi, J., Harris, A.W., 1989. Application of photometric models to asteroids. Asteroids II 52, 4–556.

Brown, P.G., Assink, J.D., Astiz, L., et al., 2013. Nature 503, 238. http://dx.doi.org/10.1038/nature12741.

Brown, P., Spalding, R.E., ReVelle, D.O., Tagliaferri, E., Worden, S.P., 2002. The flux of small near-earth objects colliding with the earth. Nature 420, 294–296. http://dx.doi.org/10.1038/nature01238.

Brown, P., Wiegert, P., Clark, D., Tagliaferri, E., 2016. Orbital and physical characteristics of meter-scale impactors from airburst observations. Icarus 266, 96–111. http://dx.doi.org/10.1016/j.icarus.2015.11.022.

Christensen, E., et al., 2012. The catalina sky survey: Current and future work. In: AAS/Division for Planetary Sciences Meeting Abstracts #44.

Daubar, I.J., et al., 2022. Current impact cratering on mars, seen AND heard! In: AAS/Division for Planetary Sciences Meeting Abstracts.

Deienno, et al., 2023. NEO model from ATLAS. in preparation.

Dohnanyi, J.S., 1969. Collisional model of asteroids and their debris. J. Geophys. Res. 74, 2531–2554. http://dx.doi.org/10.1029/JB074i010p02531.

Ďurech, J., Hanuš, J., 2023. Reconstruction of asteroid spin states from gaia DR3 photometry. Astron. Astrophys. 675. http://dx.doi.org/10.1051/0004-6361/202345889.

Eugster, O., Herzog, G.F., Marti, K., Caffee, M.W., 2006. Irradiation records, cosmic-ray exposure ages, and transfer times of meteorites. Meteorit. Early Solar Syst. II 829.

Farnocchia, D., Chesley, S.R., Vokrouhlický, D., Milani, A., Spoto, F., Bottke, W.F., 2013. Near earth asteroids with measurable yarkovsky effect. Icarus 224, 1–13. http://dx.doi.org/10.1016/j.icarus.2013.02.004.

Feroz, F., Hobson, M.P., 2008. Multimodal nested sampling: an efficient and robust alternative to Markov chain Monte Carlo methods for astronomical data analyses. Mon. Not. R. Astron. Soc. 384, 449–463. http://dx.doi.org/10.1111/j.1365-2966.2007.12353.x.

Feroz, F., Hobson, M.P., Bridges, M., 2009. MULTINEST: an efficient and robust Bayesian inference tool for cosmology and particle physics. Mon. Not. R. Astron. Soc. 398, 1601–1614. http://dx.doi.org/10.1111/j.1365-2966.2009.14548.x.

Gaia Collaboration, et al., 2018. Gaia data release 2. Summary of the contents and survey properties. Astron. Astrophys. 616. http://dx.doi.org/10.1051/0004-6361/201833051.

Gaia Collaboration, et al., 2023. Gaia data release 3. Summary of the content and survey properties. Astron. Astrophys. 674. http://dx.doi.org/10.1051/0004-6361/202243940.

Granvik, M., Brown, P., 2018. Identification of meteorite source regions in the solar system. Icarus 311, 271–287. http://dx.doi.org/10.1016/j.icarus.2018.04.012.

Granvik, M., Walsh, K.J., 2017. Thermal and tidal destruction of near-earth objects. In: European Planetary Science Congress.

Granvik, M., Walsh, K., 2022. Near-earth asteroids destroyed by tidal forces during planetary flybys. In: AAS/Division for Planetary Sciences Meeting Abstracts.

Granvik, M., Walsh, K., 2023. Tidal disruption of near-earth asteroids during close encounters with terrestrial planets. arXiv e-prints, https://doi.org/10.48550/arXiv.2312.08247.

Granvik, M., et al., 2016. Super-catastrophic disruption of asteroids at small perihelion distances. Nature 530, 303–306. http://dx.doi.org/10.1038/nature16934.

Granvik, M., et al., 2018. Debiased orbit and absolute-magnitude distributions for near-earth objects. Icarus 312, 181–207. http://dx.doi.org/10.1016/j.icarus.2018.04.018.

Harris, A.W., Chodas, P.W., (HC21), 2021. The population of near-earth asteroids revisited and updated. Icarus 365. http://dx.doi.org/10.1016/j.icarus.2021.114452.

Harris, A.W., Chodas, P.W., 2023. Update of NEA population and survey completion. In: ACM Conference in Flagstaff. https://www.hou.usra.edu/meetings/acm2023/pdf/2519.pdf.

Harris, A.W., D'Abramo, G., 2015. The population of near-earth asteroids. Icarus 257, 302–312. http://dx.doi.org/10.1016/j.icarus.2015.05.004.

Hartmann, W.K., 2005. Martian cratering 8: Isochron refinement and the chronology of mars. Icarus 174, 294–320. http://dx.doi.org/10.1016/j.icarus.2004.11.023.

Heinze, A.N., et al., 2021. NEO population, velocity bias, and impact risk from an ATLAS analysis. Planet. Sci. J. 2. http://dx.doi.org/10.3847/PSJ/abd325.

Jedicke, R., Bolin, B., Granvik, M., Beshore, E., 2016. A fast method for quantifying observational selection effects in asteroid surveys. Icarus 266, 173–188. http://dx.doi.org/10.1016/j.icarus.2015.10.021.

Krietsch, D., Busemann, H., Riebe, M.E.I., King, A.J., Alexander, C.M.O., Maden, C., 2021. Noble gases in CM carbonaceous chondrites: Effect of parent body aqueous and thermal alteration and cosmic ray exposure ages. Geochim. Cosmochim. Acta 310, 240–280. http://dx.doi.org/10.1016/j.gca.2021.05.050.

La Spina, A., Paolicchi, P., Kryszczyńska, A., Pravec, P., 2004. Retrograde spins of near-earth asteroids from the yarkovsky effect. Nature 428, 400–401. http://dx.doi.org/10.1038/nature02411.

Mainzer, A.K., et al., 2019. NEOWISE diameters and albedos V2.0. NASA Planet. Data Syst. http://dx.doi.org/10.26033/18S3-2Z54.

Marchi, S., 2021. A new martian crater chronology: Implications for jezero crater. Astron. J. 161. http://dx.doi.org/10.3847/1538-3881/abe417.

Morbidelli, A., Gladman, B., 1998. Orbital and temporal distributions of meteorites originating in the asteroid belt. Meteorit. Planet. Sci. 33, 999–1016. http://dx.doi.org/10.1111/j.1945-5100.1998.tb01707.x.

Naidu, S.P., Chesley, S.R., Farnocchia, D., 2017. Near-earth object survey simulation software. In: AAS/Division for Planetary Sciences Meeting Abstracts #49.

Nesvorný, D., Bottke, W.F., Marchi, S., 2021. Dark primitive asteroids account for a large share of K/Pg-scale impacts on the earth. Icarus 368. http://dx.doi.org/10.1016/j.icarus.2021.114621.

Nesvorný, D., Brož, M., Carruba, V., 2015. Identification and dynamical properties of asteroid families. Asteroids IV 297–321. http://dx.doi.org/10.2458/azu_uapress_9780816532131-ch016.

Nesvorný, D., et al., 2023. NEOMOD: A new orbital distribution model for near-earth objects. Astron. J. 166. http://dx.doi.org/10.3847/1538-3881/ace040.

Neukum, G., Ivanov, B.A., Hartmann, W.K., 2001. Cratering records in the inner solar system in relation to the lunar reference system. Space Sci. Rev. 96, 55–86. http://dx.doi.org/10.1023/A:1011989004263.

Popova, O., Nemtchinov, I., Hartmann, W.K., 2003. Bolides in the present and past martian atmosphere and effects on cratering processes. Meteorit. Planet. Sci. 38, 905–925. http://dx.doi.org/10.1111/j.1945-5100.2003.tb00287.x.

Pravec, P., Harris, A.W., 2000. Fast and slow rotation of asteroids. Icarus 148, 12–20. http://dx.doi.org/10.1006/icar.2000.6482.

Pravec, P., Harris, A.W., Kušnirák, P., Galád, A., Hornoch, K., 2012. Absolute magnitudes of asteroids and a revision of asteroid albedo estimates from WISE thermal observations. Icarus 221, 365–387. http://dx.doi.org/10.1016/j.icarus.2012.07.026.

Press, W.H., Teukolsky, S.A., Vetterling, W.T., Flannery, B.P., 1992. Numerical Recipes in C. The Art of Scientific Computing, second ed. University Press, Cambridge, p. c1992.

Richardson, D.C., Bottke, W.F., Love, S.G., 1998. Tidal distortion and disruption of earth-crossing asteroids. Icarus 134, 47–76. http://dx.doi.org/10.1006/icar.1998.5954.

Silber, E.A., ReVelle, D.O., Brown, P.G., et al., 2009. J. Geophys. Res. (Planets) 114, E08006. http://dx.doi.org/10.1029/2009JE003334.

Skilling, J., 2004. Nested sampling. In: Bayesian Inference and Maximum Entropy Methods in Science and Engineering: 24th International Workshop on Bayesian Inference and Maximum Entropy Methods in Science and Engineering, Vol. 735. pp. 395–405. http://dx.doi.org/10.1063/1.1835238.

Speyerer, E.J., Wagner, R.V., Povilaitis, R.Z., Robinson, M.S., Martin, A.C., Denevi, B.W., 2020. Constraining the contemporary impact cratering rate and understanding the impact process with temporal and photometric observations. In: 51st Annual Lunar and Planetary Science Conference.

Stuart, J.S., 2001. A near-earth asteroid population estimate from the LINEAR survey. Science 294, 1691–1693. http://dx.doi.org/10.1126/science.1065318.

Tricarico, P., 2016. Detection efficiency of asteroid surveys. Astron. J. 151. http://dx.doi.org/10.3847/0004-6256/151/3/80.

Tricarico, P., 2017. The near-earth asteroid population from two decades of observations. Icarus 284, 416–423. http://dx.doi.org/10.1016/j.icarus.2016.12.008.

Vokrouhlický, D., Bottke, W.F., Chesley, S.R., Scheeres, D.J., Statler, T.S., 2015. The yarkovsky and YORP effects. Asteroids IV 509–531. http://dx.doi.org/10.2458/azu_uapress_9780816532131-ch027.

Vokrouhlický, D., Farinella, P., 2000. Efficient delivery of meteorites to the earth from a wide range of asteroid parent bodies. Nature 407, 606–608. http://dx.doi.org/10.1038/35036528.

Vokrouhlický, D., Nesvorný, D., Bottke, W.F., 2003. The vector alignments of asteroid spins by thermal torques. Nature 425, 147–151. http://dx.doi.org/10.1038/nature01948.

Wisdom, J., 2017. Meteorite transport—revisited. Meteorit. Planet. Sci. 52, 1660–1668. http://dx.doi.org/10.1111/maps.12876.